PTEP

Prog. Theor. Exp. Phys. **2017**, 123D04 (27 pages)
DOI: 10.1093/ptep/ptx163

Predicting $K^0\Lambda$ photoproduction observables by using the multipole approach

T. Mart* and A. Rusli

Departemen Fisika, FMIPA, Universitas Indonesia, Depok 16424, Indonesia
*E-mail: terry.mart@sci.ui.ac.id

Received April 25, 2017; Revised October 28, 2017; Accepted October 29, 2017; Published December 23, 2017

We present an isobar model for kaon photoproduction on the proton $\gamma p \to K^+\Lambda$ that can nicely reproduce the available experimental data from threshold up to $W = 2.0$ GeV. The background amplitude of the model is constructed from a covariant Feynman diagrammatic method, whereas the resonance one is formulated by using the multipole approach. All unknown parameters in both background and resonance amplitudes are extracted by adjusting the calculated observables to experimental data. With the help of SU(3) isospin symmetry and some information obtained from the Particle Data Group we estimate the cross section and polarization observables for the neutral kaon photoproduction on the neutron $\gamma n \to K^0\Lambda$. The result indicates no sharp peak in the $K^0\Lambda$ total cross section. The predicted differential cross section exhibits resonance structures only at $\cos\theta = -1$. To obtain sizable observables the present work recommends measurement of the $K^0\Lambda$ cross section with $W \gtrsim 1.70$ GeV, whereas for the recoiled Λ polarization measurement with $W \approx 1.65$–1.90 GeV would be advised, since the predictions of existing models show a large variance at this kinematics. The predicted electric and magnetic multipoles are found to be mostly different from those obtained in previous works. For $W = 1.75$ and 1.95 GeV it is found that most of the single and double polarization observables demonstrate large asymmetries.

Subject Index D32

1. Introduction

The earliest theoretical investigation of kaon photoproduction based on a covariant Feynman diagrammatic approach was performed nearly 60 years ago [1]. The first experimental measurement that produced about three citable data points was also done in the same year [2]. Today, 60 years later, thanks to the significant development in accelerator and detector technologies, we have nearly 20 000 data points for kaon photoproduction on both protons and neutrons with unprecedented accuracy. Note that the experimental data of photoproduction on neutrons were extracted from a deuteron target, since a neutron cannot be used as a stable target.

There are six isospin channels in kaon photoproduction on the nucleon, i.e.,

$$\gamma + p \to K^+ + \Lambda,$$
$$\gamma + p \to K^+ + \Sigma^0,$$
$$\gamma + p \to K^0 + \Sigma^+,$$
$$\gamma + n \to K^0 + \Lambda,$$
$$\gamma + n \to K^+ + \Sigma^-,$$
$$\gamma + n \to K^0 + \Sigma^0.$$

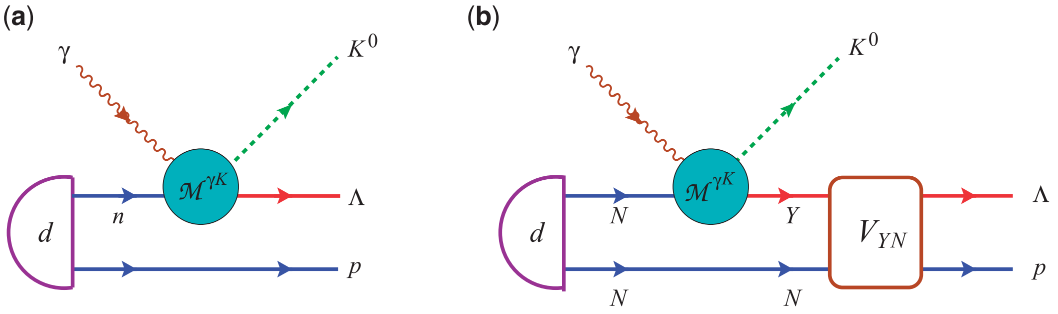

Fig. 1. Neutral kaon photoproduction on the deuteron: (a) in the impulse approximation and (b) with the *YN* rescattering process.

The presently available experimental data are dominated by the $\gamma p \to K^+\Lambda$ and $\gamma p \to K^+\Sigma^0$ channels, because these two channels are relatively simple to measure. There are much fewer data points available for the $\gamma p \to K^0\Sigma^+$ channel [3], although this channel is also accessible by using the present technology. In fact, data with very high statistics to this end have been collected by the CLAS Collaboration and are currently being analyzed (R. A. Schumacher, private communication).

In the neutron channel, there are also very limited data points for the $\gamma n \to K^+\Sigma^-$ isospin channel taken by the LEPS [4] and CLAS [5] Collaborations. We note that the use of modern techniques in those experiments has made it possible to measure this channel with relatively high accuracy.

Photoproduction of the neutral kaon on the neutron ($K^0\Lambda$ or $K^0\Sigma^0$) is more difficult than photoproduction of the kaon on the proton ($K^+\Lambda$, $K^+\Sigma^0$, or $K^0\Sigma^+$), since in the former the final state contains two neutral particles and the target cannot be a free neutron. To this end, the photoproduction of neutral kaon on a deuteron has been experimentally performed at the LNS Tohoku University [6]. A new attempt to provide a more accurate result has been performed at the same laboratory by the FOREST Collaboration and the final result will be published soon [7]. To extract the $K^0\Lambda$ cross section from this experiment we could in principle use the simple impulse approximation, as depicted in Fig. 1(a). However, for a more accurate result we should also include the hyperon–nucleon rescattering process, as shown in Fig. 1(b). In the latter, along with the precise *YN* potential, we desperately need the precise information on the $K^0\Sigma^0$ and $K^0\Sigma^+$ amplitudes [8,9].

Since extracting the $K^0\Lambda$ cross section from kaon photoproduction on the deuteron could become a daunting task, we have to look for another mechanism that can harness the available information provided by the other isospin channels, especially the $K^+\Lambda$ channel for which the experimental data are abundant. For this purpose we can use the isospin symmetry relation of the coupling constants for the background terms and the available photon helicity amplitudes $A_{1/2}$ and $A_{3/2}$ provided by the Particle Data Group (PDG) in the Review of Particle Properties (RPP) [10] for the resonance terms.

The purpose of this paper is to present the results of our work in predicting the $K^0\Lambda$ photoproduction observables by using the multipole approach. For this purpose we have to extract the scattering amplitude for the $\gamma p \to K^+\Lambda$ process by fitting the available experimental data, which are relatively abundant at present, to the calculated observables. The scattering amplitude for the $\gamma n \to K^0\Lambda$ channel can be predicted by exploiting the isospin symmetry along with the neutron helicity amplitudes obtained from the PDG.

We have started this calculation by focusing the energy range of our investigation near the threshold region [11,12]. A recent phenomenological investigation of the $K^0\Sigma^0$ and $K^+\Sigma^-$ photoproductions near their threshold energies has also been reported [13]. The present work provides an extension of our previous work, which was valid only near the threshold region [12], to the total center-of-mass (c.m.) energy $W \approx 2.0$ GeV. A preliminary result of this work has been presented at a conference [14].

We organize this paper as follows. The background and resonance amplitudes used in the present investigation are explained in Sect. 2. In Sect. 3 we briefly discuss the nucleon resonances included in the present work as well as the experimental data used in our database. Section 4 contains a discussion on the result of fitting the $K^+\Lambda$ channel and the prediction of the $K^0\Lambda$ channel. Since at present only the Kaon-Maid model [15–18][1] provides prediction of the $K^0\Lambda$ channel, we will compare the result obtained in the present work with the prediction of Kaon-Maid. Finally, we will summarize and conclude our findings in Sect. 5.

2. The background and resonance amplitudes

In principle, the background and resonance amplitudes used in the present work can be found in our previous work [19–21]. Nevertheless, for the convenience of the reader we will briefly summarize these amplitudes in the following.

The momenta of photon and hadron are defined by the $K^+\Lambda$ photoproduction process,

$$\gamma(k) + p(p) \rightarrow K^+(q) + \Lambda(p_\Lambda) \, , \tag{1}$$

from which we can calculate the required Mandelstam variables:

$$s \;=\; (k+p)^2 = W^2 \;\; , \quad t \;=\; (k-q)^2 \;\; , \quad u \;=\; (k-p_\Lambda)^2. \tag{2}$$

The Mandelstam variable u is actually fixed by the on-shell condition $s + t + u = \sum_i m_i^2$. The corresponding momenta for the $K^0\Lambda$ process are defined in a similar way to Eq. (1).

The scattering amplitude can be divided into two parts, i.e., the background and resonance parts. The background part is constructed from the appropriate Feynman diagrams for the s-, t-, and u-channel Born terms along with the $K^{*+}(892)$, $K_1(1270)$ vector mesons in the t-channel and the $\Lambda(1405)S_{01}$, $\Lambda(1600)P_{01}$, $\Lambda(1670)S_{01}$, $\Lambda(1800)S_{01}$, $\Lambda(1810)P_{01}$, $\Sigma(1660)P_{11}$, and $\Sigma(1750)S_{11}$ hyperon resonances in the u-channel. These diagrams are shown in Fig. 2 for the $\gamma p \rightarrow K^+\Lambda$ process. For the $\gamma n \rightarrow K^0\Lambda$ process we use the same diagrams, but we replace the charged particles with neutral ones, i.e., $p \rightarrow n$, $K^+ \rightarrow K^0$, and $K^{*+} \rightarrow K^{*0}$.

By using the pseudoscalar coupling the background amplitude for kaon photoproduction on a proton shown in Fig. 2 can be written as [11]

$$\begin{aligned}
\mathcal{M}^{\gamma K}_{\text{back.}} = \bar{u}_\Lambda(\boldsymbol{p}_\Lambda)\biggl[& i g_{K\Lambda N}\, F^p(s)\, \gamma_5 \, \frac{\not{p} + \not{k} + m_p}{s - m_p^2} \, \left(\not{\epsilon} e + i\sigma^{\mu\nu}\epsilon_\mu k_\nu \mu_p\right) \\
& + i\sigma^{\mu\nu}\epsilon_\mu k_\nu \mu_\Lambda \, \frac{\not{p}_\Lambda - \not{k} + m_\Lambda}{u - m_\Lambda^2} \, i g_{K\Lambda N}\, F^\Lambda(u)\, \gamma_5 + i e g_{K\Lambda N}\, F^K(t)\, \gamma_5 \, \frac{(2q_K - k)\cdot\epsilon}{t - m_K^2} \\
& + \frac{ie\, F^{K^*}(t)}{M(t - m_{K^*}^2 + i m_{K^*}\Gamma_{K^*})} \left\{ G^V_{K^*}\gamma_\mu - \frac{G^T_{K^*}}{m_p + m_\Lambda} i\sigma^{\mu\nu}(q_K - k)_\nu \right\} i\varepsilon_{\mu\nu\rho\sigma}\epsilon^\nu k^\rho q_K^\sigma \\
& + \frac{e\, F^{K_1}(t)}{M(t - m_{K_1}^2 + i m_{K_1}\Gamma_{K_1})} \, \{ G^V_{K_1}\gamma^\mu\gamma_5 + \frac{G^T_{K_1}}{m_p + m_\Lambda}(\not{p}_\Lambda - \not{p})\gamma^\mu\gamma_5 \biggr\}
\end{aligned}$$

---

[1] For the online version of Kaon-Maid, see Ref. [15]; published versions include Refs. [16–18].

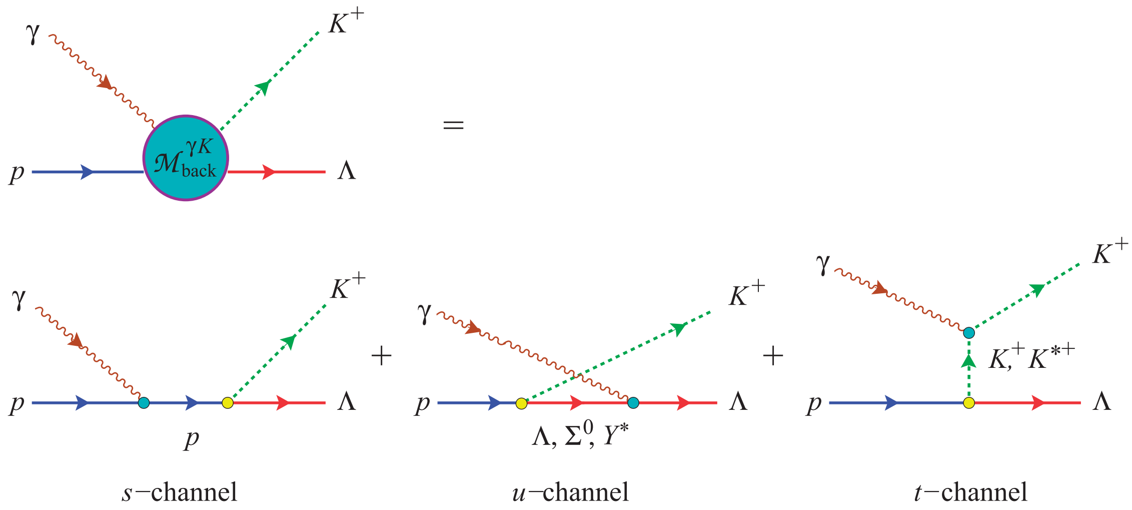

Fig. 2. Feynman diagrams used for the background amplitude in the $\gamma p \to K^+\Lambda$ process. In the case of the $\gamma n \to K^0\Lambda$ process the corresponding diagrams are similar, except with the replacements $p \to n$, $K^+ \to K^0$, and $K^{*+} \to K^{*0}$.

$$\times\left\{(q_K - k)\cdot\epsilon\, k_\mu - (q_K - k)\cdot k\,\epsilon_\mu\right\}$$

$$+\, i\sigma^{\mu\nu}\epsilon_\mu k_\nu \frac{\not p_\Sigma - \not k + m_\Sigma}{u - m_\Sigma^2}\,\frac{ie\kappa_T F^\Sigma(u)}{m_\Lambda + m_\Sigma}\, g_{K\Sigma N}\,\gamma_5$$

$$+\, i\sigma^{\mu\nu}\epsilon_\mu k_\nu \frac{\not p_{Y^*} - \not k + m_{Y^*}}{u - m_{Y^*}^2 + i m_{Y^*}\Gamma_{Y^*}}\,\frac{ieF^{Y^*}(u)}{m_\Lambda + m_{Y^*}}\, G_{Y^*}\gamma_5\Bigg]\, u_p(\boldsymbol{p}_p), \tag{3}$$

where we have defined $G^{(V,T)}_{K^*} \equiv g^{(V,T)}_{K^*\Lambda N}\, g_{K^*K\gamma}$, $G^{(V,T)}_{K_1} \equiv g^{(V,T)}_{K_1\Lambda N}\, g_{K_1K\gamma}$, $G_{Y^*} = \kappa_{Y^*}\, g_{KY^*N}$, and κ_T is the transition anomalous moment. Furthermore, ϵ indicates the polarization vector of the photon, μ_p and μ_Λ are the proton and Λ magnetic moments, respectively, $M = 1$ GeV is introduced to make the K^* and K_1 coupling constants dimensionless since the numerator of the vector meson amplitude contains an extra momentum dependence, and $F^i(x)$ is the hadronic form factor of the i intermediate state with $x = s, t$, or u.

The hadronic form factors $F^i(x)$ are considered in all hadronic vertices because all hadrons in the background part are composite objects. In the present work we use the dipole form [22]

$$F^i(x) = \frac{\Lambda_{\rm B}^4}{\Lambda_{\rm B}^4 + \left(x - m_i^2\right)^2}, \qquad x = s, u, \text{ or } t, \tag{4}$$

where the hadronic cutoff $\Lambda_{\rm B}$ is considered as a free parameter. Note that the background amplitude given in Eq. (3) is not gauge invariant due to the fact that the contributions of the s- and t-channels in Fig. 2 are not individually gauge invariant and their hadronic form factors are different for different diagrams. To restore the gauge invariance of this amplitude we use the Haberzettl prescription [22].

The resonance part is obtained by parameterizing the electric $E_{\ell\pm}$ or magnetic $M_{\ell\pm}$ multipoles with the help of the Breit–Wigner formula [19,23,24],

$$A_{\ell\pm}(W) = \bar{A}_{\ell\pm}\, c_{K\Lambda}\, \frac{f_{\gamma R}(W)\,\Gamma_{\rm tot}(W) m_R f_{KR}(W)}{m_R^2 - s - i m_R \Gamma_{\rm tot}(W)}\, e^{i\varphi}, \tag{5}$$

where $\bar{A}_{\ell\pm}$ denotes the electric $E_{\ell\pm}$ or magnetic $M_{\ell\pm}$ multipole photon couplings, $c_{K\Lambda}$ is the isospin factor, φ indicates the resonance phase, m_R is the physical mass of the resonance and $\Gamma_{\rm tot}(W)$ is the energy-dependent resonance total width, which is given by [23]

$$\Gamma_{\rm tot}(W) \;=\; \Gamma_{KY}(W) + \Gamma_{\rm in}(W), \tag{6}$$

with the energy-dependent partial width [23]

$$\Gamma_{KY}(W) = \beta_K \Gamma_R \left(\frac{|\boldsymbol{q}|}{q_R}\right)^{2\ell+1} \left(\frac{X^2+q_R^2}{X^2+\boldsymbol{q}^2}\right)^{\ell} \frac{W_R}{W}, \tag{7}$$

and the "inelastic" width [23]

$$\Gamma_{\rm in}(W) \;=\; (1-\beta_K)\Gamma_R \left(\frac{q_\pi}{q_0}\right)^{2\ell+4} \left(\frac{X^2+q_0^2}{X^2+q_\pi^2}\right)^{\ell+2}, \tag{8}$$

where β_K is the single kaon branching ratio, Γ_R and q_R are the total width and kaon c.m. momentum calculated at $W = M_R$, q_π denotes the momentum of the pion in the decay process $R \to \pi + N$ in the c.m. system, and q_0 is q_π calculated at $W = m_R$. In the present work we use the damping parameter $X = 500$ MeV for all resonances [19,23].

The Breit–Wigner factor f_{KR} in Eq. (5) is given by [23,24]

$$f_{KR}(W) = \left[\frac{1}{(2j+1)\pi}\frac{k_W}{|\boldsymbol{q}|}\frac{m_N}{W}\frac{\Gamma_{KY}}{\Gamma_{\rm tot}^2}\right]^{1/2}, \tag{9}$$

with

$$k_W \;=\; \frac{W^2-m_N^2}{2W}, \tag{10}$$

and the contribution of the γNR vertex to the electric and magnetic multipoles $f_{\gamma R}$ is parameterized by using [23]

$$f_{\gamma R} = \left(\frac{k_W}{k_R}\right)^{2\ell'+1} \left(\frac{X^2+k_R^2}{X^2+k_W^2}\right)^{\ell'}, \tag{11}$$

where k_R is equal to k_W given by Eq. (10) but calculated at $W = M_R$. For the multipoles $M_{\ell\pm}$ and $E_{\ell+}$ we have $\ell' = \ell$, whereas for the electric multipoles $E_{\ell-}$ we have $\ell' = \ell - 2$ if $\ell \geq 2$ [25].

For $j = \ell + 1/2$ the electric $E_{\ell+}$ and magnetic $M_{\ell+}$ multipoles given in Eq. (5) can be written in terms of the helicity amplitudes $A_{1/2}$ and $A_{3/2}$ as [19,24]

$$E_{\ell+} = \frac{1}{\ell+1}\left[-A_{1/2}^{\ell+} + \sqrt{\frac{\ell}{\ell+2}}\,A_{3/2}^{\ell+}\right], \tag{12}$$

$$M_{\ell+} = -\frac{1}{\ell+1}\left[A_{1/2}^{\ell+} + \sqrt{\frac{\ell+2}{\ell}}\,A_{3/2}^{\ell+}\right], \tag{13}$$

while for $j = (\ell+1) - 1/2$ the corresponding relations for the electric $E_{\ell-}$ and magnetic $M_{\ell-}$ multipoles read [19,24]

$$E_{(\ell+1)-} = -\frac{1}{\ell+1}\left[A_{1/2}^{(\ell+1)-} + \sqrt{\frac{\ell+2}{\ell}}\,A_{3/2}^{(\ell+1)-}\right], \tag{14}$$

$$M_{(\ell+1)-} = \frac{1}{\ell+1}\left[A_{1/2}^{(\ell+1)-} - \sqrt{\frac{\ell}{\ell+2}}\,A_{3/2}^{(\ell+1)-}\right]. \tag{15}$$

Table 1. The electric and magnetic multipoles in terms of the helicity photon amplitudes for the nucleon resonance states with the angular momentum up to $\ell = 3$ calculated from Eqs. (12)–(15). Reference [19] gives the relations for the angular momentum up to $\ell = 4$.

State	ℓ	ℓ'	Multipoles	Expression
S_{11}	0	0	E_{0+}	$-A_{1/2}^{0+}$
P_{11}	1	1	M_{1-}	$A_{1/2}^{1-}$
P_{13}	1	1	E_{1+}	$\frac{1}{2}\left(-A_{1/2}^{1+} + \sqrt{\frac{1}{3}}A_{3/2}^{1+}\right)$
	1	1	M_{1+}	$-\frac{1}{2}\left(A_{1/2}^{1+} + \sqrt{3}A_{3/2}^{1+}\right)$
D_{13}	2	0	E_{2-}	$-\frac{1}{2}\left(A_{1/2}^{2-} + \sqrt{3}A_{3/2}^{2-}\right)$
	2	2	M_{2-}	$\frac{1}{2}\left(A_{1/2}^{2-} - \sqrt{\frac{1}{3}}A_{3/2}^{2-}\right)$
D_{15}	2	2	E_{2+}	$\frac{1}{3}\left(-A_{1/2}^{2+} + \sqrt{\frac{1}{2}}A_{3/2}^{2+}\right)$
	2	2	M_{2+}	$-\frac{1}{3}\left(A_{1/2}^{2+} + \sqrt{2}A_{3/2}^{2+}\right)$
F_{15}	3	1	E_{3-}	$-\frac{1}{3}\left(A_{1/2}^{3-} + \sqrt{2}A_{3/2}^{3-}\right)$
	3	3	M_{3-}	$\frac{1}{3}\left(A_{1/2}^{3-} - \sqrt{\frac{1}{2}}A_{3/2}^{3-}\right)$

The relevant multipoles for the present work are listed in Table 1. Further explanation of these parameters is given in detail in Refs. [19,20,23]. The number and type of nucleon resonances included in our present model will be explained in Sect. 3.

To calculate the observables the background and resonance amplitudes can be combined in the form of Chew–Goldberger–Low–Nambu (CGLN) amplitudes [26]:

$$F = i\mathcal{F}_1\, \boldsymbol{\sigma} \cdot \boldsymbol{\epsilon} + \mathcal{F}_2\, \boldsymbol{\sigma} \cdot \hat{\boldsymbol{q}}\, \boldsymbol{\sigma} \cdot (\hat{\boldsymbol{k}} \times \boldsymbol{\epsilon}) + i\mathcal{F}_3\, \boldsymbol{\sigma} \cdot \hat{\boldsymbol{k}}\, \hat{\boldsymbol{q}} \cdot \boldsymbol{\epsilon} + i\mathcal{F}_4\, \boldsymbol{\sigma} \cdot \hat{\boldsymbol{q}}\, \hat{\boldsymbol{q}} \cdot \boldsymbol{\epsilon}. \tag{16}$$

As in the previous studies [11,13,19], the background amplitudes can be decomposed into four CGLN amplitudes $\mathcal{F}_i$ of Eq. (16), i.e., [28,29]

$$\mathcal{M}_{\text{back.}} = \chi_{\text{f}}^{\dagger}\, F\, \chi_{\text{i}}. \tag{17}$$

On the other hand, the resonance electric $E_{\ell\pm}$ or magnetic $M_{\ell\pm}$ multipoles given by Eq. (5) can be related to the CGLN amplitudes $\mathcal{F}_i$ of Eq. (16) by expanding the amplitudes in terms of the derivatives of Legendre polynomials [26–28]:

$$\mathcal{F}_1 = \sum_{\ell \geq 0} \left\{ (\ell M_{\ell+} + E_{\ell+})\, P'_{\ell+1}(x) + [(\ell+1)\, M_{\ell-} + E_{\ell-}]\, P'_{\ell-1}(x) \right\}, \tag{18}$$

$$\mathcal{F}_2 = \sum_{\ell \geq 1} [(\ell+1)\, M_{\ell+} + \ell M_{\ell-}]\, P'_{\ell}(x), \tag{19}$$

$$\mathcal{F}_3 = \sum_{\ell \geq 1} \left[(E_{\ell+} - M_{\ell+})\, P''_{\ell+1}(x) + (E_{\ell-} + M_{\ell-})\, P''_{\ell-1}(x) \right], \tag{20}$$

$$\mathcal{F}_4 = \sum_{\ell \geq 2} (M_{\ell+} - E_{\ell+} - M_{\ell-} - E_{\ell-})\, P''_{\ell}(x), \tag{21}$$

where $x = \cos\theta$ and θ is the kaon scattering angle in the c.m. frame.

Table 2. Breit–Wigner parameters of the nucleon resonances used in the present work taken from the Review of Particle Properties (RPP) of the Particle Data Group (PDG) [10]. The units for the photon helicity amplitudes of the proton and neutron are 10^{-3} GeV$^{-1/2}$. Unless indicated otherwise, the listed data are estimates of the PDG. See the body text and the Review on Nucleon and Delta Resonances section of the RPP [10] for further explanation.

State	m_R (MeV)	Γ_R (MeV)	β_K ($\times 10^{-3}$)	$A_{1/2}(p)$	$A_{3/2}(p)$	$A_{1/2}(n)$	$A_{3/2}(n)$	Overall status
$N(1650)S_{11}$	1645 to 1670	110 to 170	50 to 150	45 ± 10	–	-50 ± 20	–	****
$N(1710)P_{11}$	1680 to 1740	50 to 250	50 to 250	50 ± 10^a	–	-40 ± 20^b	–	****
$N(1720)P_{13}$	1700 to 1750	150 to 400	43 ± 4^c	100 ± 20	135 ± 40^a	-80 ± 50^b	-140 ± 65^b	****
$N(1900)P_{13}$	1900 ± 30	200 ± 50	20 to 200	24 ± 14^a	-67 ± 30^a	0 ± 30^b	-60 ± 45^b	***
$N(1700)D_{13}$	1650 to 1750	100 to 250	–	41 ± 17^b	-37 ± 14^a	25 ± 10^b	-32 ± 18^b	***
$N(1875)D_{13}$	1820 to 1920	250 ± 70	2 ± 2^d	18 ± 10^e	-7 ± 4^a	10 ± 6^b	-20 ± 15^b	***
$N(1675)D_{15}$	1670 to 1680	130 to 165	–	19 ± 8	20 ± 5	-60 ± 5	-85 ± 10	****
$N(1680)F_{15}$	1680 to 1690	120 to 140	–	-15 ± 6	133 ± 12	29 ± 10	-33 ± 9	****

[a] Taken from Ref. [30].
[b] Taken from Ref. [31].
[c] Taken from Ref. [32].
[d] Taken from Ref. [33].
[e] Taken from Ref. [34].

In general, to calculate the observables the background and resonance amplitudes can be combined by inserting a phase angle ζ between the two amplitudes, i.e.,

$$\mathcal{F}_i^{\text{tot}} = \mathcal{F}_i^{\text{back.}}\, e^{i\zeta} + \mathcal{F}_i^{\text{res}}. \tag{22}$$

However, for the sake of simplicity, in the present work we only consider $\zeta = 0$. Finally, the cross section and polarization observables can be written in terms of $\mathcal{F}_i^{\text{tot}}$. To this end, the complete formulas are given, e.g., in Ref. [28].

3. The nucleon resonances and experimental data

To predict the amplitudes of the $\gamma n \to K^0\Lambda$ channel we need information on the neutron helicity amplitudes $A_{1/2}(n)$ and $A_{3/2}(n)$. By scrutinizing the nucleon resonance properties provided by the PDG [10] it is found that only the well established nucleon resonances (those with a three- or four-star rating) have the estimated values of the neutron helicity amplitudes.

To simplify the model we also limit the energy range of the analyzed data up to $W = 2$ GeV. As a result only 8 nucleon resonances can contribute to the model, as listed in Table 2. These resonances will be used in both $K^+\Lambda$ and $K^0\Lambda$ models. As a consequence, the values of orbital angular momentum ℓ given in Eqs. (5) and (18)–(21) are limited only up to $\ell = 3$. Should we extend the energy range of interest to $W = 2.8$ GeV, as in our recent analysis [35], the number of involved nucleon resonances turns out to be 20. In this case the upper value of ℓ is 7, whereas the relations between the electric and magnetic multipoles to the helicity amplitudes $A_{1/2}$ and $A_{3/2}$, comparable to the PDG listing [10], for $\ell \leq 7$ are given in Table I of Ref. [36]. Therefore, the formulation of nucleon resonances in the present work can be considered as a subset of the more general formulation given in Ref. [36].

By limiting the energy range of interest to below $W = 2$ GeV the number of available experimental data reduces to 3587. This is less than 50% of the total available data used in our recent analysis [35]. Since the number of fitted parameters is also significantly reduced by limiting the number of nucleon resonances, the quality of fitting, i.e., the value of χ^2 per number of degrees of freedom ($\chi^2/N_{\rm dof}$), is expected to be comparable to the result of our recent analysis, i.e., $\chi^2/N_{\rm dof} = 1.63$. Note that the number of degrees of freedom is defined as $N_{\rm dof} = N_{\rm data} - N_{\rm par}$, where $N_{\rm data}$ and $N_{\rm par}$ are the number of experimental data and fitted parameters, respectively. χ^2 is defined as usual,

$$\chi^2 = \sum_{i=1}^{N_{\rm data}} \left\{ \frac{\sigma_i({\rm exp}) - \sigma_i({\rm th})}{\Delta\sigma_i({\rm exp})} \right\}^2 , \tag{23}$$

where σ_i(exp) and $\Delta\sigma_i$(exp) are the ith experimental observable (differential cross section or polarization observable) and its error bar, while σ_i(th) is the corresponding theoretical calculation. In the experimental error bars besides the statistical errors we have also included the systematic uncertainties. The minimization process was performed by using the MINUIT code [40]. To obtain the best result we performed the minimization by using the SIMPLEX and MIGRAD minimizers until the MIGRAD output reached convergence. The crude SIMPLEX minimizer is required to quickly find the direction of the minimum before we feed the fitting parameters into the more accurate MIGRAD minimizer, which produces the parameter values given in the following section. A more detailed explanation about MINUIT and MIGRAD minimizers can be found in Ref. [40].

4. Results and discussion

4.1. The $K^+\Lambda$ channel

As stated in the introduction we must obtain the scattering amplitude for the $\gamma p \to K^+\Lambda$ channel before we can predict the observables of the $\gamma n \to K^0\Lambda$ channel. To this end we have fitted the coupling constants and hadronic form factor cutoff in the background terms and the resonance parameters, i.e., the resonance mass m_R, the total width Γ_R, the kaon branching ratio β_K, the helicity amplitudes $A_{1/2}(p)$ and $A_{3/2}(p)$, and the resonance phase φ, in the resonance terms. During the fitting process the leading coupling constants, $g_{K\Lambda N}/\sqrt{4\pi}$ and $g_{K\Sigma N}/\sqrt{4\pi}$, were constrained by the SU(3) symmetry [29,37]. Furthermore, to keep the order of magnitude of the coupling constants at unity we have limited the variation of the coupling constants between -10 and 10. The result is shown in Table 3 for the background parameters and Table 4 for the resonance parameters.

From Table 3 it is apparent that the leading coupling constants obtained in the present work are only slightly different from those in the previous covariant model [20]. Two of the extracted hyperon resonance coupling constants, $G_{\Lambda(1810)}$ and $G_{\Sigma(1600)}$, are at their lower limit. A similar finding has also been reported by previous studies [20,38].

It was demonstrated that the huge contribution of the Born terms can be significantly reduced by including certain hyperon resonances [39]. Note that in the previous covariant isobar model [20] (see the fourth column of Table 3) and Kaon-Maid [15–18] the cutoff values are relatively small. In Kaon-Maid the cutoffs are $\Lambda_{\rm B} = 0.64$ GeV for the $K\Lambda$ channels and $\Lambda_{\rm B} = 0.82$ GeV for the $K\Sigma$ channels.

In the present work, to investigate the influence of hyperon resonances, we have also run our fit without the hyperon resonances. In Table 3 we list the background coupling constants obtained if these resonances are removed. Of course we understand that the impact is not only exerted on the background coupling constants, but also on all resonance parameters, as shown in Table 4. Table 3 shows that without these resonances the χ^2 increases significantly. However, unlike the previous work [20], in the present model the inclusion of hyperon resonances does not affect the hadronic

Table 3. The background parameters (coupling constants and hadronic form factor cutoff Λ_B) and the value of $\chi^2/N_{\rm dof}$ obtained from fitting to experimental data in the present work compared with those obtained in the covariant isobar model (the best model, i.e., model D in Ref. [20]). The number of degrees of freedom is defined as $N_{\rm dof} = N_{\rm data} - N_{\rm par}$.

	Present		
Parameter	with Y^*	without Y^*	Covariant
$g_{K\Lambda N}/\sqrt{4\pi}$	-3.00	-3.00	-3.00
$g_{K\Sigma N}/\sqrt{4\pi}$	0.90	0.90	1.27
$G^V_{K*}/4\pi$	-0.06	-0.13	0.15
$G^T_{K*}/4\pi$	0.14	0.16	0.26
$G^V_{K_1}/4\pi$	0.16	0.37	1.46
$G^T_{K_1}/4\pi$	-1.97	-1.88	0.07
$G_{\Lambda_{1405}}/4\pi$	-0.81	–	–
$G_{\Lambda_{1600}}/4\pi$	6.18	–	8.41
$G_{\Lambda_{1670}}/4\pi$	2.48	–	–
$G_{\Lambda_{1800}}/4\pi$	0.73	–	–
$G_{\Lambda_{1810}}/4\pi$	-10.00	–	-9.61
$G_{\Sigma_{1600}}/4\pi$	-9.99	–	–
$G_{\Sigma_{1750}}/4\pi$	1.07	–	–
Λ_B (GeV)	1.51	1.52	0.70
$N_{\rm data}$	3587	3587	7433
$N_{\rm par}$	60	53	96
$\chi^2/N_{\rm dof}$	1.32	1.40	1.58

cutoff. Furthermore, we also note that in both models (fitting with and without hyperon resonances) the cutoffs are significantly larger than those obtained in the previous covariant model [20].

Table 4 lists the resonance parameters extracted from fitting to experimental data with and without the hyperon resonances, where the available PDG estimates [10] are also displayed for comparison. Note that during the fitting process these parameters were only allowed to vary within the PDG error bars. Except for a number of kaon branching ratios β_K, where no estimates have been provided by the PDG, from Table 4 we may conclude that all extracted parameters in both models can be constrained within the PDG values.

The result of the present work shown in the second and third columns of Table 3 obviously does not corroborate the previous finding [39], because the cutoff is relatively large in both models, i.e., $\Lambda_B \approx 1.50$ GeV. Presumably, the effect of excluding the hyperon resonances is compensated by the changes of nucleon resonance parameters. As shown in Table 4, for certain nucleon resonances the parameters could significantly change if the hyperon resonances were excluded.

Nevertheless, the effect of hyperon resonances on the background amplitude is not completely negligible. As shown in Table 3, the inclusion of hyperon resonances decreases most of the meson resonance coupling constants. The effect of hyperon resonances on the background contribution to the total cross section can be seen in Fig. 3, where it is obvious that by including the hyperon resonances the background contribution decreases by 10–20%. Interestingly, in both models of the present work the background contribution increases significantly for $W \gtrsim 1.85$ GeV, while the background contribution of the extended model [35] decreases slightly. This behavior originates from the large hadronic cutoff obtained in the present work, $\Lambda_B \approx 1.50$ GeV. At relatively high energies, i.e., $W \gtrsim 1.90$ GeV, such a cutoff is unable to suppress the diverging background contribution. In the extended model the hadronic form factor is much softer, i.e., $\Lambda_B \approx 0.65$ GeV. We also note that

Table 4. The extracted nucleon resonance parameters from fitting to experimental data in the present work with hyperon resonances (PW1) and without hyperon resonances (PW2), compared with the estimates of the PDG [10]. The units for the photon helicity amplitudes are 10^{-3} GeV$^{-1/2}$.

Resonance (Status)	Data from	m_R (MeV)	Γ_R (MeV)	β_K (10^{-3})	$A_{1/2}(p)$	$A_{3/2}(p)$	φ (deg.)
$N(1650)S_{11}$	PW1	1670	143	79	55	–	202
(****)	PW2	1665	132	58	55	–	195
	PDG	1645–1670	110–170	50–150	45 ± 10	–	–
$N(1710)P_{11}$	PW1	1707	176	50	40	–	95
(****)	PW2	1720	174	50	40	–	107
	PDG	1680–1740	50–250	50–250	50 ± 10	–	–
$N(1720)P_{13}$	PW1	1722	400	39	80	95	271
(****)	PW2	1700	400	39	80	95	264
	PDG	1700–1750	150–400	43 ± 4	100 ± 20	135 ± 40	–
$N(1900)P_{13}$	PW1	1930	250	125	34	-68	246
(***)	PW2	1930	246	162	34	-58	246
	PDG	1900 ± 30	200 ± 50	20–200	24 ± 14	-67 ± 30	–
$N(1700)D_{13}$	PW1	1650	100	0	24	-51	132
(***)	PW2	1750	100	1	24	-51	237
	PDG	1650–1750	100–250	–	41 ± 17	-37 ± 14	–
$N(1875)D_{13}$	PW1	1920	320	4	28	-11	38
(***)	PW2	1920	180	4	28	-11	80
	PDG	1820–1920	250 ± 70	2 ± 2	18 ± 10	-7 ± 4	–
$N(1675)D_{15}$	PW1	1680	130	3	27	15	348
(****)	PW2	1680	136	6	27	15	357
	PDG	1670–1680	130–165	–	19 ± 8	20 ± 5	–
$N(1680)F_{15}$	PW1	1690	140	0	-21	121	248
(****)	PW2	1690	120	0	-9	145	225
	PDG	1680–1690	120–140	–	-15 ± 6	133 ± 12	–

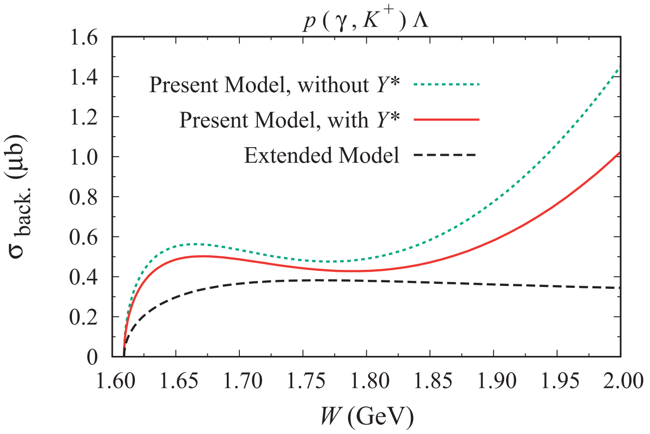

Fig. 3. Background contribution to the total cross section of the $\gamma p \to K^+\Lambda$ channel. The dashed line shows the background of the extended model that is valid up to $W = 2.8$ [35], the dotted line exhibits the background contribution of the present work if the contribution of all hyperon resonances is switched off, and the solid line displays the background contribution of the present work if all hyperon resonances listed in Table 3 are included.

Table 5. Contribution of the individual χ^2/N from different observables $\mathcal{O}$ obtained from fitting with and without hyperon resonances. In the second column $\chi^2_{\mathcal{O}}$ is the value of χ^2 calculated only with the data of observable $\mathcal{O}$, while $N_{\mathcal{O}}$ is the number of data of observable $\mathcal{O}$.

	$\chi^2_{\mathcal{O}}/N_{\mathcal{O}}$	
Observable $\mathcal{O}$	with Y^*	without Y^*
$d\sigma/d\Omega$	0.99	1.07
P	1.21	1.30
Σ	2.82	4.08
T	4.17	3.37
C_x	1.23	1.31
C_z	4.19	4.52
$O_{x'}$	2.78	2.57
$O_{z'}$	4.93	4.40

the diverging nature of the background as shown in Fig. 3 is essentially attributed to the fact that the present models do not satisfy the unitarity of the S-matrix.

It is important to remind the reader that all included hyperon resonances in the present work listed in Table 3 have spin $J = 1/2$. Thus, a detailed study on the contribution of hyperon resonances with spins $J \geq 3/2$ is strongly required at present, because their contribution can be expected to produce a destructive interference with the Born terms, so that the hadronic form factor cutoff can be further increased. This is not only important in the present study, but also in other tree-level isobar models of meson photoproduction. For this purpose we have studied the effects of spin-3/2 and spin-5/2 hyperon resonances in kaon photoproduction. The result will be reported elsewhere [44]. At this stage, it is worth mentioning that the contribution of hyperon resonances is also crucial to enhance the performance of the model, especially in the case of angular distributions.

In Table 5 we show the values of χ^2/N for each observable used in our fitting database. It is clear that different observables have different χ^2/N contributions. However, in general we can say that an observable with a large number of data has a strong influence on the fit result, especially if the data have small error bars. Therefore, it is understandable that the differential cross section and recoil polarization have the smallest χ^2/N. In fact, including or excluding the hyperon resonances does not change this result.

For the sake of simplicity and since the agreement with experimental data is better, in what follows we will use the model that includes the hyperon resonances. Figure 4(a) compares the total cross sections obtained from the present and previous works with experimental data. Obviously, the agreement of the present model calculation with experimental data is better than those of the covariant isobar [20] and Kaon-Maid [15–18] models. This finding is consistent because the value of $\chi^2/N_{\rm dof}$ obtained in the present work is smaller than those obtained in the covariant isobar [20] and Kaon-Maid [15–18] models, even though the total cross section data shown in Fig. 4(a) were not included in the fitting database.

Figure 4(a) also shows that the present model can nicely reproduce the first and second peaks, where a number of established nucleon resonances contribute. Furthermore, the behavior of Kaon-Maid is as expected, because this model was fitted to the SAPHIR 1998 data [54], which have the problem of data consistency for $W \gtrsim 1.75$ GeV. Note that this problem has been extensively discussed in the past [19,56,57].

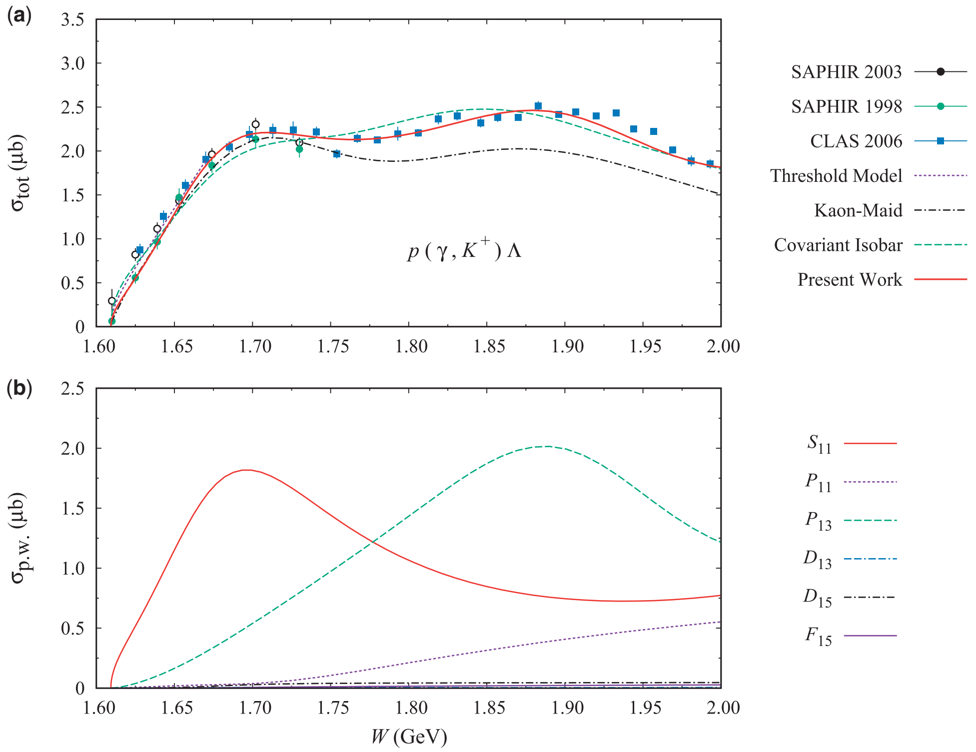

Fig. 4. (a) Calculated total cross sections obtained from the present work (solid curve) compared with the covariant isobar model (dashed curve) [20], Kaon-Maid model (dash-dotted curve) [15–18], and a simple model that works only near the threshold [11]. Experimental data taken from the CLAS 2006 (solid squares) [45], SAPHIR 1998 (solid circles) [54], and SAPHIR 2003 (open circles) [55] Collaborations were not included in the fitting database. These data are displayed here just for comparison. (b) Contribution of each partial wave to the $K^+\Lambda$ total cross section of the present work.

To shed more information on the role of each partial wave in the present model in Fig. 4(b) we show the contribution of individual partial waves to the total cross section shown in Fig. 4(a). Note that the partial waves shown in Fig. 4(b) include the background contribution. Since the background contribution is calculated from the covariant Feynman diagrammatic technique, we have to invert Eqs. (18)–(21) to obtain the multipoles, i.e., [26–28]

$$E_{\ell+}^{\rm back.} = \frac{1}{2(\ell+1)}\int_{-1}^{1} dx \left[P_\ell \mathcal{F}_1 - P_{\ell+1}\mathcal{F}_2 + \frac{\ell}{2\ell+1}\left(P_{\ell-1}-P_{\ell+1}\right)\mathcal{F}_3 \right.$$
$$\left. + \frac{\ell+1}{(2\ell+3)}\left(P_\ell - P_{\ell+2}\right)\mathcal{F}_4\right], \tag{24}$$

$$E_{\ell-}^{\rm back.} = \frac{1}{2\ell}\int_{-1}^{1} dx \left[P_\ell \mathcal{F}_1 - P_{\ell-1}\mathcal{F}_2 + \frac{\ell+1}{2\ell+1}\left(P_{\ell+1}-P_{\ell-1}\right)\mathcal{F}_3 \right.$$
$$\left. + \frac{\ell}{(2\ell-1)}\left(P_\ell - P_{\ell-2}\right)\mathcal{F}_4\right], \tag{25}$$

$$M_{\ell+}^{\rm back.} = \frac{1}{2(\ell+1)}\int_{-1}^{1} dx \left[P_\ell \mathcal{F}_1 - P_{\ell+1}\mathcal{F}_2 + \frac{1}{2\ell+1}\left(P_{\ell+1}-P_{\ell-1}\right)\mathcal{F}_3\right], \tag{26}$$

$$M_{\ell-}^{\rm back.} = \frac{1}{2\ell}\int_{-1}^{1} dx \left[-P_\ell \mathcal{F}_1 + P_{\ell-1}\mathcal{F}_2 + \frac{1}{2\ell+1}\left(P_{\ell-1}-P_{\ell+1}\right)\mathcal{F}_3\right], \tag{27}$$

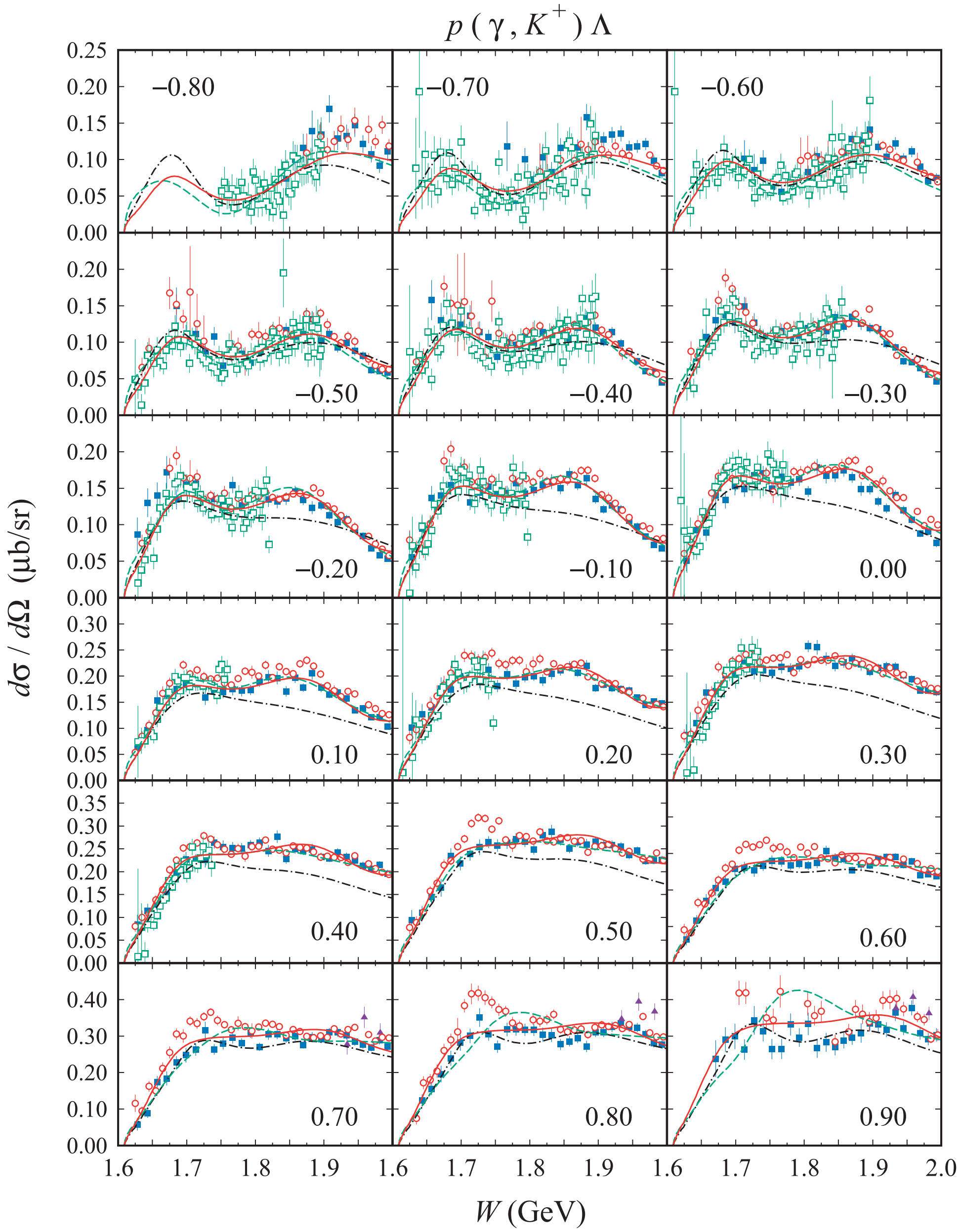

Fig. 5. Differential cross sections as a function of the total c.m. energy W for different values of $\cos\theta$, where θ is the kaon scattering angle in the c.m. system. Experimental data are from the CLAS 2006 (solid squares) [45], CLAS 2010 (open circles) [47], LEPS 2006 (solid triangles) [51], and Crystal Ball 2014 (open squares) [48] Collaborations. Notation of the curves is as in Fig. 4(a).

where $\mathcal{F}_1, \ldots, \mathcal{F}_4$ are the CGLN amplitudes given by Eq. (16) for the background terms. These multipoles are added to the resonance ones to obtain the contribution of each partial wave to the total cross section shown in Fig. 4(b).

Obviously the structure of the total cross section shown in Fig. 4(a) can be understood from the contribution of each partial wave shown in Fig. 4(b). The largest contribution near the threshold region originates from the S_{11} partial wave that peaks near $W \approx 1.65$–1.70 GeV. At higher energy the largest contribution comes from the P_{13} partial wave. From Table 4 we would expect the structures of two states, i.e., at $W \approx 1.70$ and 1.90 GeV. However, since the kaon branching ratio for the state

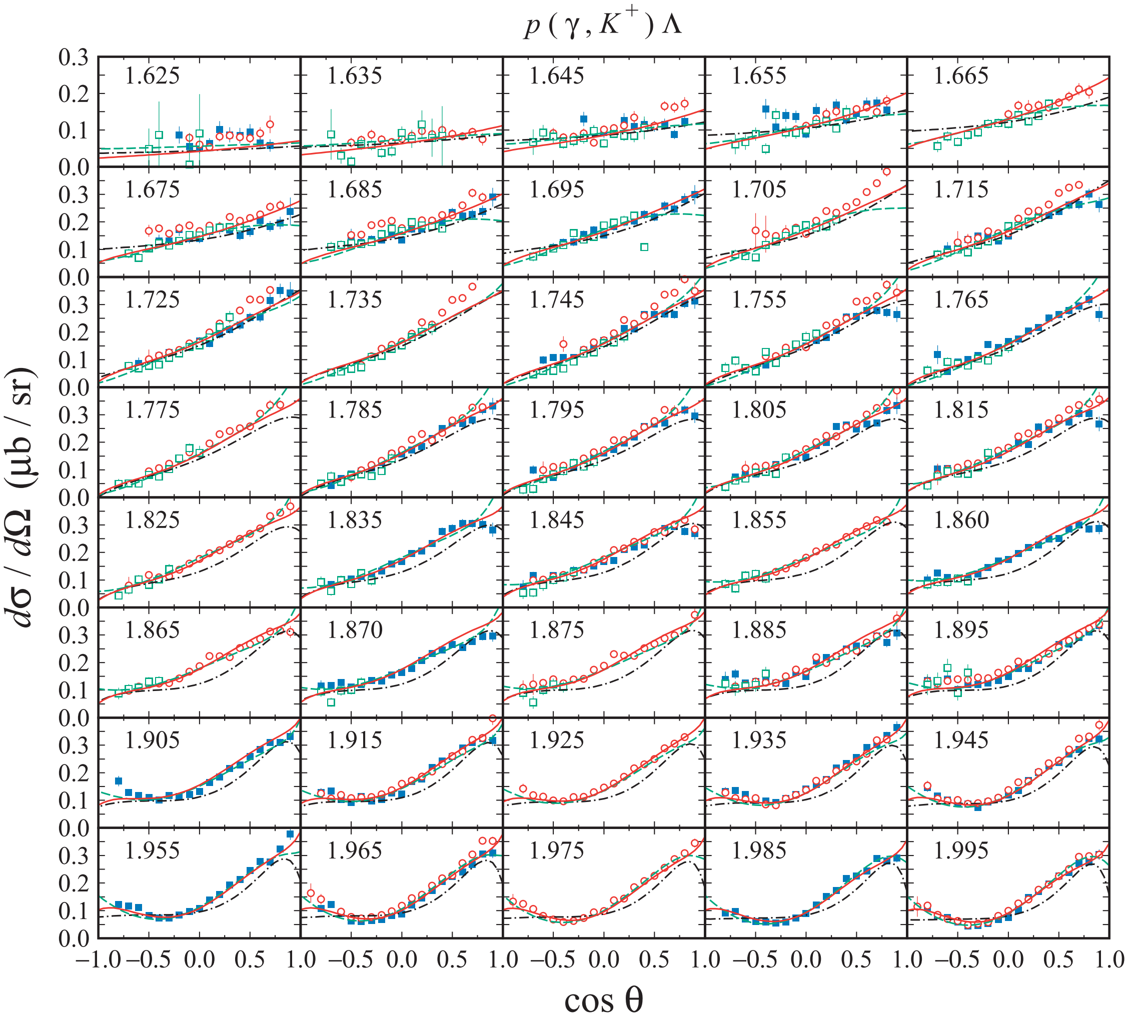

Fig. 6. As in Fig. 5, but for angular distributions.

at $W \approx 1.70$ GeV is relatively small, the P_{13} partial wave contribution reaches its maximum at $W \approx 1.90$ GeV. A relatively smaller, but still sizable, contribution is obtained for the P_{11} partial wave. As shown in Fig. 4(b) the contribution of this partial wave is monotonically increasing as the energy increases, which indicates a typical contribution of the background. From Table 4 it is clear that the kaon branching ratio β_K for the P_{11} state at $W \approx 1.70$ GeV is not too small and as a consequence we would also expect a small structure near 1.70 GeV. However, we observe a destructive interference with the contribution from the background amplitude that eliminates this structure.

However, it is important to remember that the total cross section shown in Fig. 4(a) does not give all required and important information to reveal the physics of the process, especially when the available data for comparison are very limited, as in the present case. Therefore, the differential cross section is more valuable, notably if the physics that we are looking for depends on the angular distribution.

Exhibited in Fig. 5 is the energy distribution of the differential cross section to this end, where we display a comparison as in Fig. 4(a). We note that there are two newer data sets for the differential cross section, i.e., from the CLAS 2010 [47] and Crystal Ball 2014 [48] Collaborations. Small discrepancies between these data can be observed in Fig. 5. These discrepancies seem to be increasing as $\cos\theta$ increases in the forward direction. As shown in Fig. 5, the largest discrepancy is observed

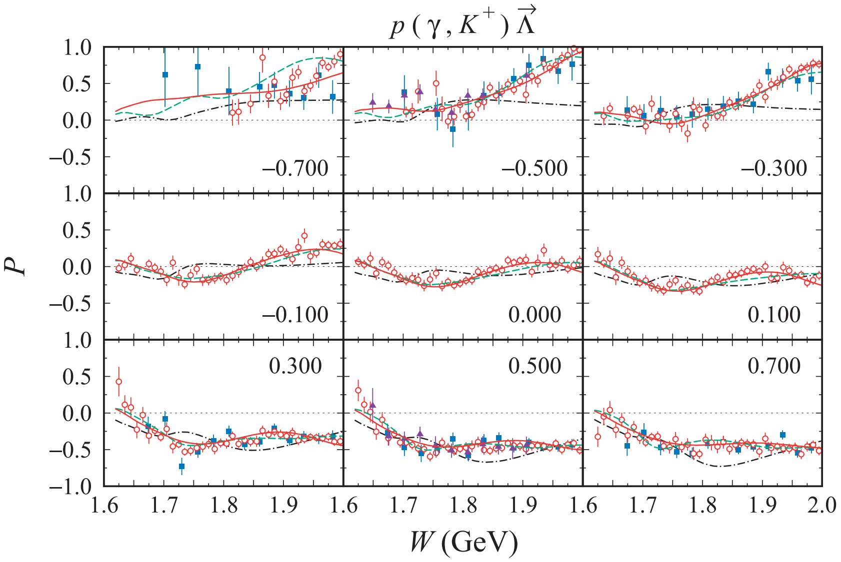

Fig. 7. Polarization of the recoiled Λ as a function of the total c.m. energy W for different values of $\cos\theta$. Experimental data are from the CLAS 2006 (solid squares) [45], CLAS 2010 (open circles) [47], GRAAL 2007 (solid triangles) [46] Collaborations. Notation of the curves is as in Fig. 4(a).

for $\cos\theta = 0.90$. This is a very unfortunate situation, because at this kinematics many important physics can be investigated, e.g., the photoproduction of the hypernucleus, given that the nuclear cross section is relatively large only at this kinematics. Since the value of $t - m_K^2$ is minimum at this kinematics, where t is the Mandelstam variable, the contribution of the t-channel resonances is at a maximum at this kinematics. Therefore, this kinematics provides a suitable means for investigating the contribution of kaon and kaon resonance exchanges in kaon photoproduction. Such a study would be very useful for the investigation of electromagnetic kaon form factors, since the signal coming from these form factors is usually very weak [12,52].

As shown by almost all panels of Fig. 5, especially those near the forward direction, to minimize the value of χ^2 the fit tries to reproduce the CLAS 2006 data, rather than the CLAS 2010 data. As a consequence the present model can nicely reproduce the CLAS 2006 total cross section as discussed above, although the number of CLAS 2010 and Crystal Ball 2014 data is not small.

The angular distribution of the differential cross section shown in Fig. 6 emphasizes the result of our previous discussion. As shown by the upper panels of Fig. 6 the data discrepancies become significant at low energies and forward angles. The present model exhibits a more forward peaking cross section in the whole energy region, compared to the other two models. This result corroborates the experimental data. Interestingly, however, the agreement with experimental data at $W \approx 1.7$ GeV becomes worse. The reason for this is that the fit tries to reproduce the forward angle data at $W = 1.715$ and 1.725 GeV, which are certainly much smaller than the other data.

We notice that a suitable experiment for resolving the problem discussed above could be carried out at the SPring8 near Osaka by the LEPS Collaboration, since the LEPS detector is built and optimized for detecting particles at forward angles. The challenging task is probably to reduce the beam energy to around $W = 1.7$ GeV, since the present data discrepancy is observed at this kinematics.

The energy and angular distributions of the recoiled Λ polarization are shown in Figs. 7 and 8, respectively. Obviously, the present model can nicely reproduce the data, except those at $W = 1.625$ GeV, as clearly shown in Fig. 8. We believe that measurement of the Λ polarization at this kinematics

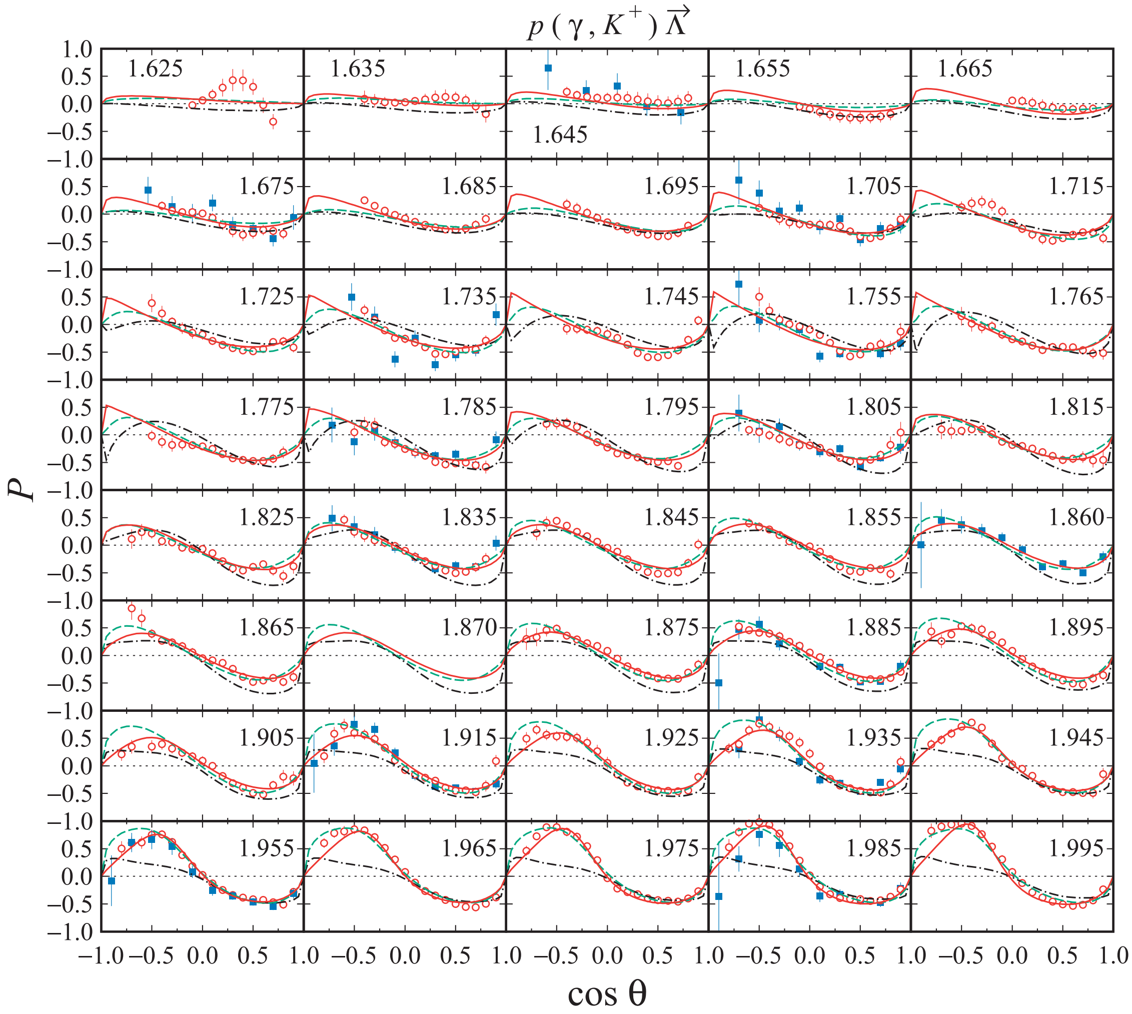

Fig. 8. As in Fig. 7, but for the angular distribution of the Λ recoil polarization with different values of the total c.m. energy W given in GeV.

should become an important agenda in the future. The result could be expected not only to resolve the current issue at threshold, but also to reexamine the origin of the evidence of narrow resonance in kaon photoproduction [49,50].

In the case of the photon and target asymmetries (Σ and T, respectively) shown in Figs. 9 and 10, we observe that the present model can reproduce the data fairly well. The same result is also exhibited in the case of the beam-recoil double polarization observables C_x, C_z, $O_{x'}$, and $O_{z'}$, as shown in Figs. 11 and 12. This result is consistent with the corresponding $\chi^2_{\mathcal{O}}/N_{\mathcal{O}}$ for these observables, as shown in Table 5.

Therefore, we believe that the present model can nicely reproduce all experimental data in all available observables in the energy range from threshold up to $W = 2.0$ GeV. Based on this model we are going to predict all observables for the $\gamma n \to K^0\Lambda$ channel in the same energy range and angular coverage.

4.2. *The $K^0\Lambda$ channel*

The background amplitude of the $K^0\Lambda$ channel can be obtained by exploiting the SU(3) symmetry, which is valid for the SU(3) multiplets of baryons and mesons. This symmetry relates the coupling

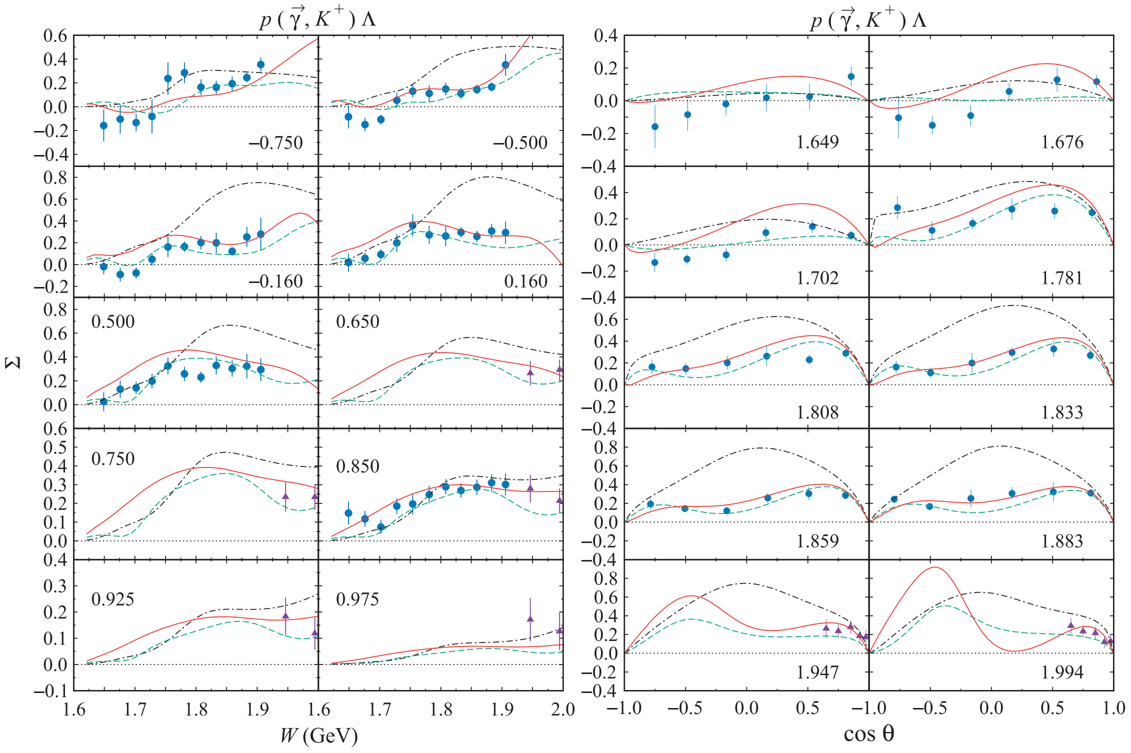

Fig. 9. Photon asymmetry as a function of the total c.m. energy and kaon angle. Notation of the curves is as in Fig. 4(a). Experimental data are from the GRAAL [46] (solid circles) and LEPS [51] (solid triangles) Collaborations.

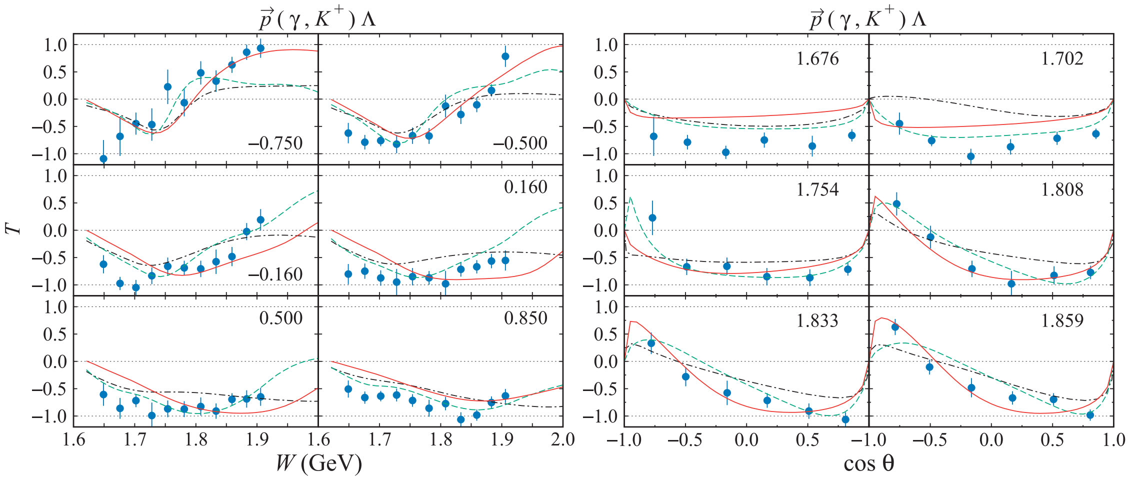

Fig. 10. Target asymmetry as a function of the total c.m. energy and kaon angle. Notation of the curves is as in Fig. 4(a). Experimental data are from the GRAAL (solid circles) [46] Collaboration.

constants in the $K^+\Lambda$ channel to those in the $K^0\Lambda$ channel. The relation of these coupling constants is given in, e.g., Refs. [12,60]. More complete relations are given in Ref. [59]. Nevertheless, for the convenience of the reader we summarize the relations below, i.e., [12,60]

$$g_{K^+\Lambda p} = g_{K^0\Lambda n}, g_{K^+\Sigma^0 p} = -g_{K^0\Sigma^0 n}, g^{V,T}_{K^{*+}\Lambda p} = g^{V,T}_{K^{*0}\Lambda n}\,. \tag{28}$$

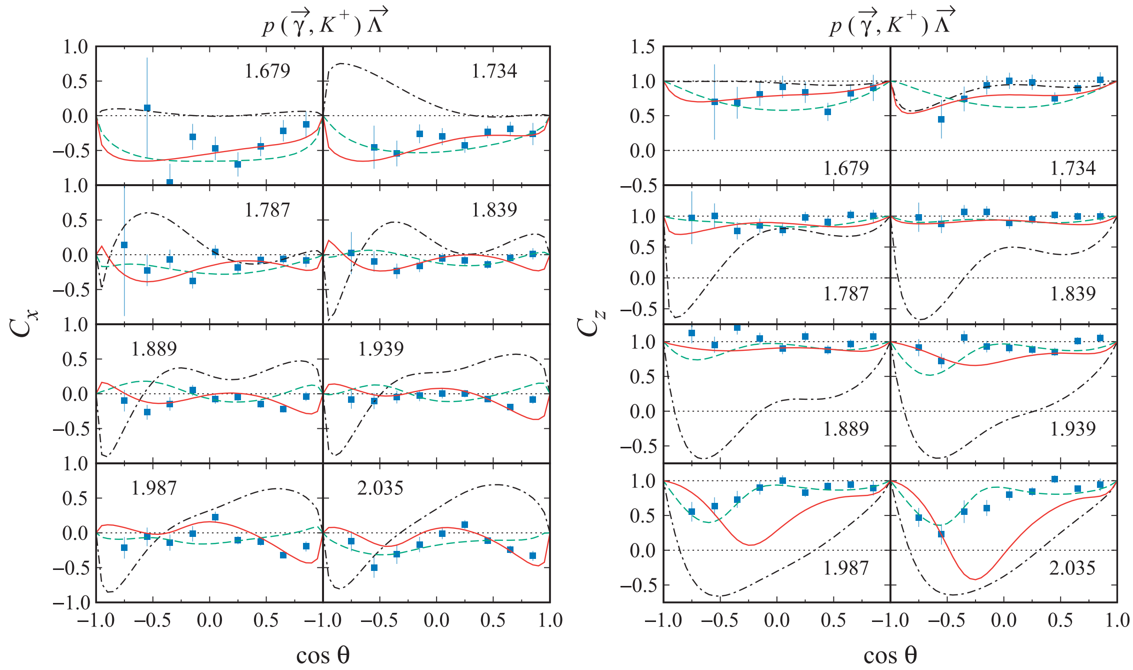

Fig. 11. The beam-recoil double polarizations C_x and C_z. Experimental data are from the CLAS Collaboration [53].

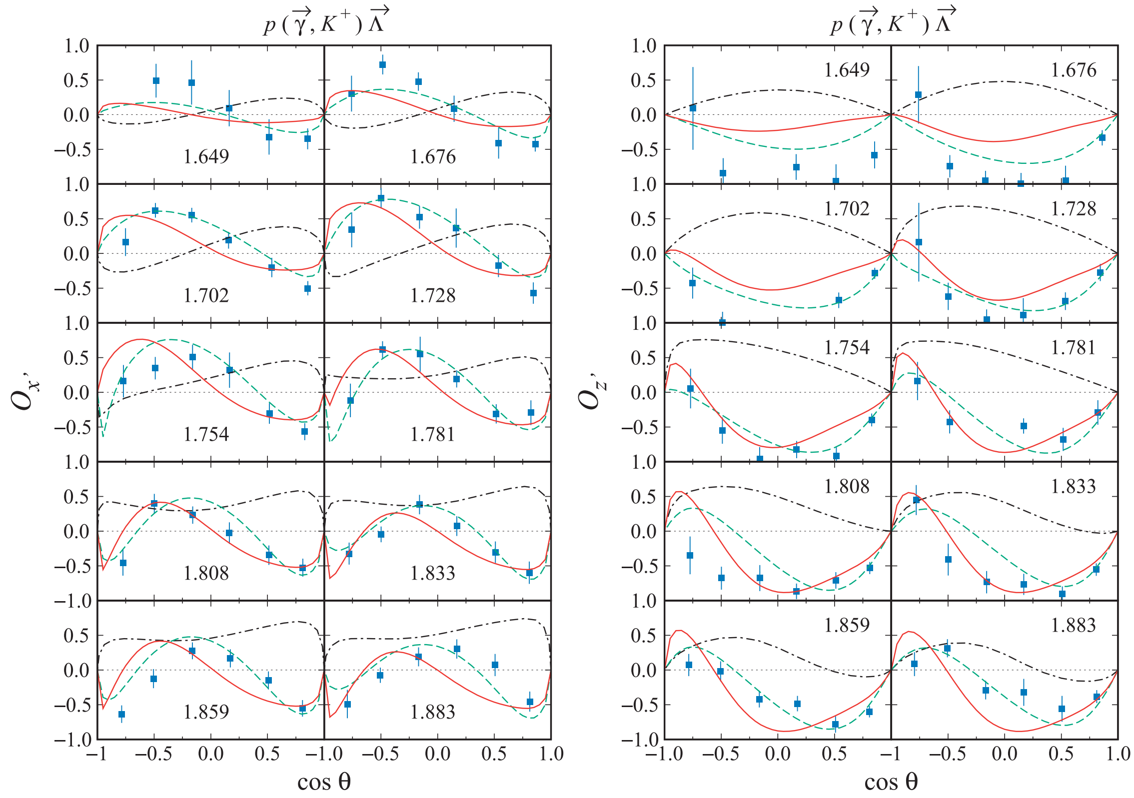

Fig. 12. As in Fig. 11, but for $O_{x'}$ and $O_{z'}$. Experimental data are from the GRAAL Collaboration [58].

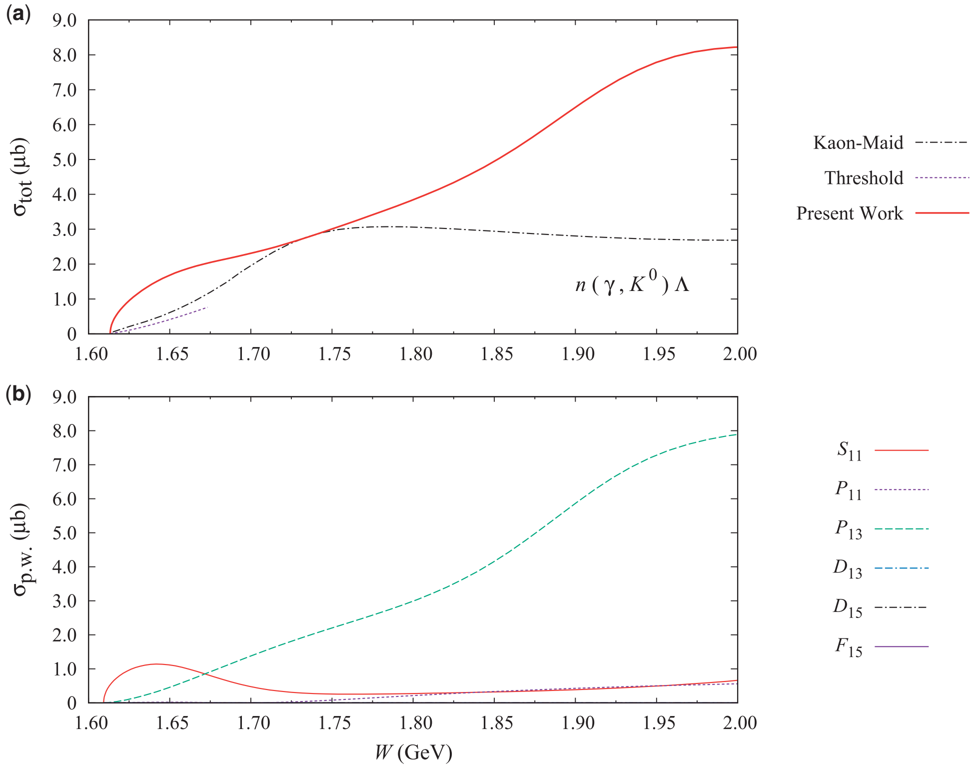

Fig. 13. (a) Total cross sections of the $K^0\Lambda$ photoproduction on the neutron predicted by Kaon-Maid (dash-dotted curve) [15–18], the previous multipole model for near-threshold production (dotted curve) [11], and the present work (solid curve). At present there are no experimental data available for comparison in this channel. (b) Contribution of each partial wave to the $K^0\Lambda$ total cross section. Note that the contributions of the D_{13}, D_{15}, and F_{15} partial waves are very small.

Furthermore, by using a quark model and the PDG values it can be shown that [12,60]

$$g_{K^{*0}K^0\gamma}/g_{K^{*+}K^+\gamma} = -1.53 \pm 0.20, g_{K_1^0K^0\gamma}/g_{K_1^+K^+\gamma} = -0.45. \tag{29}$$

For the resonance amplitude we may replace the extracted values of the helicity amplitudes of the proton $A_{1/2}(p)$ and $A_{3/2}(p)$ with those of the neutron $A_{1/2}(n)$ and $A_{3/2}(n)$ listed in Table 2. We note that the listed error bars are not small. However, in the present work we will only use the corresponding values and neglect the error bars. In other words, we predict the $K^0\Lambda$ observables by using the mean values of the PDG estimates. We believe that this is still relevant because at present we just need an estimate of the cross section and polarization observables required for proposing experiments.

The predicted $\gamma n \to K^0\Lambda$ total cross section is depicted in Fig. 13(a). Obviously the present work predicts a larger total cross section compared to our previous work that is valid very close to the threshold [11] and to the prediction of Kaon-Maid [15–18]. We note that this result originates from the large background contribution in the present work. The effect of the SU(3) relations given in Eqs. (1)–(3) of Ref. [12], therefore, produces a constructive interference that further increases the total cross section. The same phenomenon has been observed in the $K^+\Lambda$ channel (see Fig. 4(a)).

To analyze the role of different partial waves in the $K^0\Lambda$ channel we plot the contribution of the individual partial waves to the $K^0\Lambda$ total cross section in Fig. 13(b). Obviously, the P_{13} partial wave is the dominant contributor in this case. As in the case of the $K^+\Lambda$ channel shown in Fig. 4(b), the

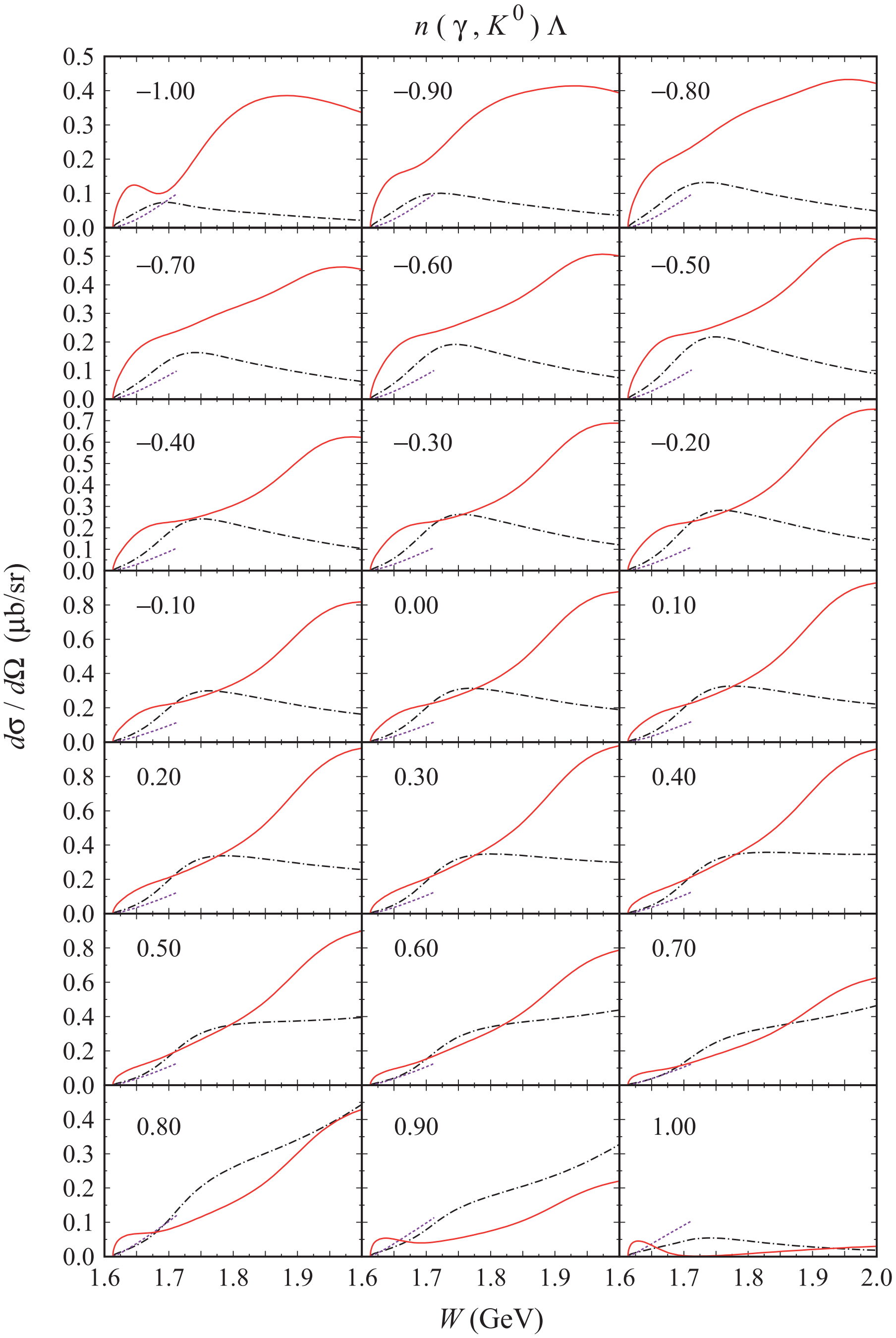

Fig. 14. The $K^0\Lambda$ differential cross sections as a function of the total c.m. energy W for different values of the kaon c.m. angle. Notation of the curves is as in Fig. 13(a).

contribution of the S_{11} partial wave is dominant near the production threshold and contribution of the P_{11} partial wave is monotonically increasing as the energy increases. Contribution from other partial waves is found to be negligible.

The energy distribution of the $\gamma n \to K^0\Lambda$ differential cross section is shown in Fig. 14, where we can clearly see the sign of resonances through two peaks. The first peak appears at $W \approx$ 1650–1680 MeV and is more pronounced at the very forward and very backward kaon angles. Obviously, this peak originates from the S_{11} partial wave contribution, as shown in Fig. 13(b). The second peak is

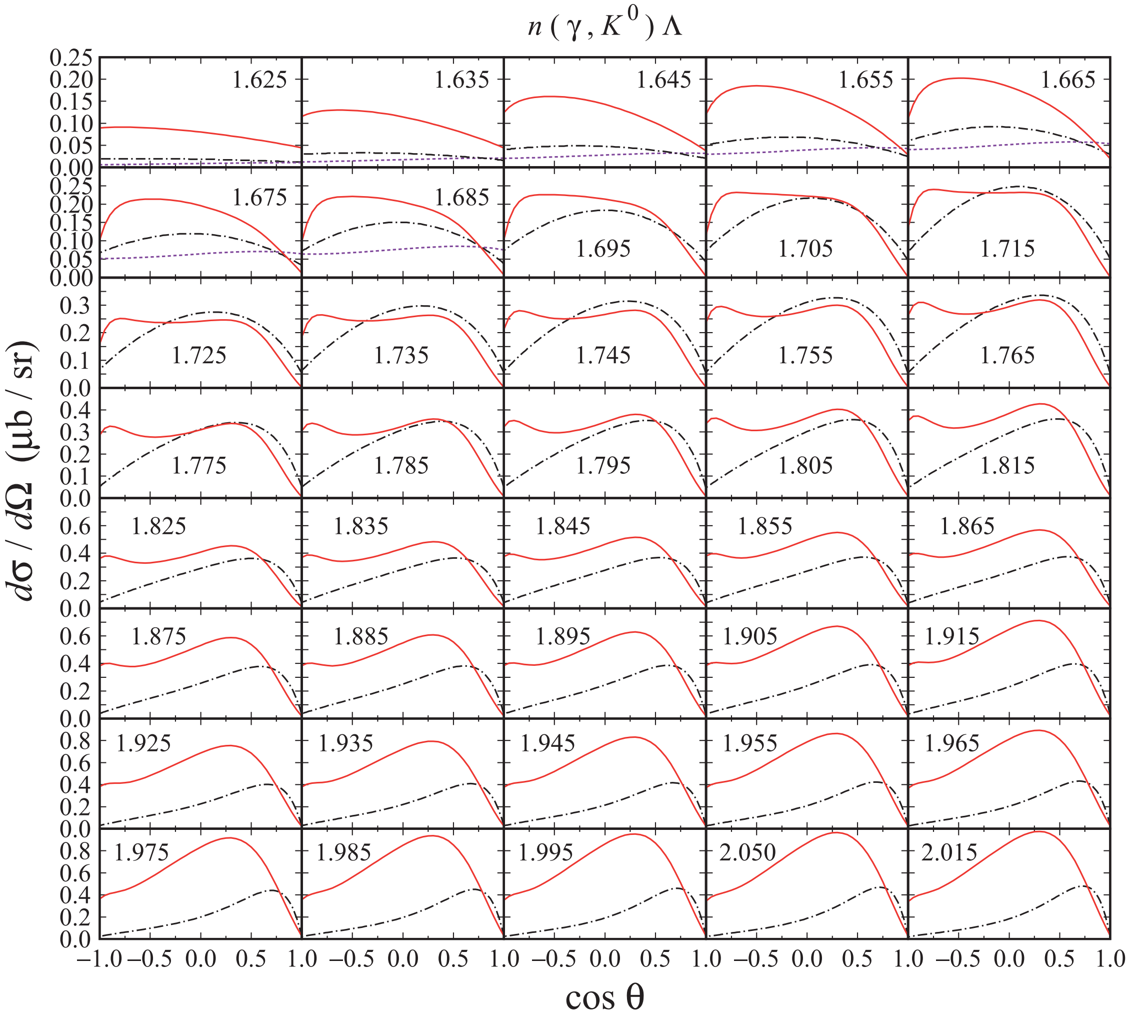

Fig. 15. As in Fig. 14, but for angular distributions.

centered at $W \approx$ 1800–2000 MeV and can only be seen at the very backward angle. The second peak disappears as we move in the direction of the forward angle. This peak originates from the contribution of the P_{13} partial wave.

The angular distribution of the differential cross section is shown in Fig. 15. Near the threshold region the differential cross section is almost forward peaking. Beyond the threshold region the shape of the cross section is almost flat, except at the very forward and backward directions. Interestingly, at higher energies the predicted cross section has a similar shape to that of Kaon-Maid [15–18], albeit with different magnitudes. The energy and angular distributions of the differential cross section shown in Figs. 14 and 15, respectively, indicate that for a sizable cross section the recommended kinematics for measurement should be $W \gtrsim 1.7$ GeV and $-0.5 \lesssim \cos\theta \lesssim 0.5$. Nevertheless, in the backward direction it would also be interesting to measure the differential cross section near the threshold region because there is a sign of the $N(1650)S_{11}$ state.

We also predict the energy and angular distributions of the recoiled Λ polarization for the $\gamma n \to K^0\Lambda$ process, as shown in Figs. 16 and 17, respectively. It is important to note at this stage that the polarization observable depends sensitively on the ingredient of the scattering amplitude. Figures 16 and 17 prove this: the discrepancy between the predictions from existing models is significantly

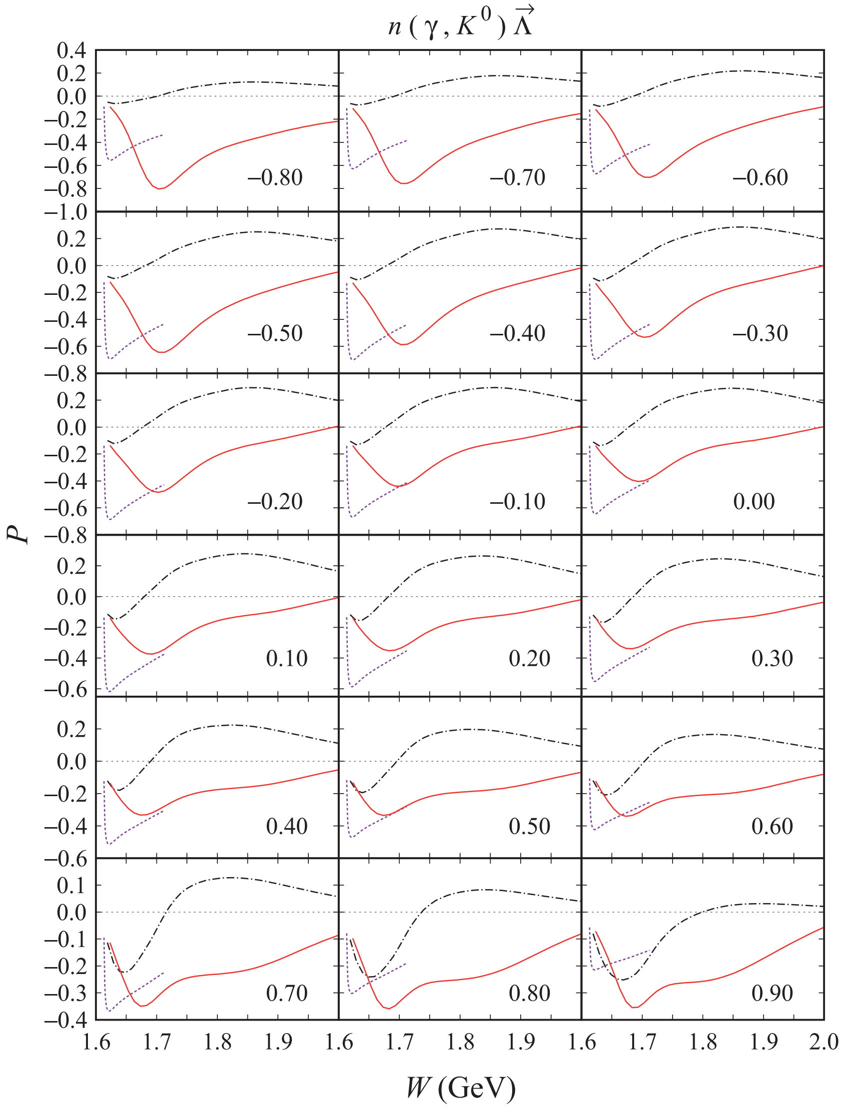

Fig. 16. Polarization of the recoiled Λ in the $\gamma n \to K^0\Lambda$ process as a function of the total c.m. energy W for different values of $\cos\theta$. The corresponding value of $\cos\theta$ is given in each panel.

large. Since these models differ in the structure of background and resonance terms, obviously the Λ polarization would serve as an important tool to reveal the most appropriate structure of the $K^0\Lambda$ photoproduction amplitude.

As in the case of the differential cross section, Figs. 16 and 17 dictate that the best measurement to this end should be focused on $W \approx 1.65$–1.90 GeV, where the variance of the existing models should be sufficiently large. The present finding is also different from the results of our previous calculations [11,15–18]. The present calculation yields a dip (inverted peak) at $W \approx 1.7$ GeV in the whole angular range, whereas Kaon-Maid shows a dip at a lower energy, i.e., $W \approx 1.65$ GeV. The result of the threshold model [11] exhibits a dip at an even lower energy. Despite their different dip positions, Fig. 16 indicates that the present work and previous calculations yield a similar shape of polarization at $W = 1.61$–1.75 GeV, as clearly shown in Fig. 17.

Figure 18 compares the electric and magnetic multipoles of the $\gamma n \to K^0\Lambda$ channel obtained from the present work with those obtained from Kaon-Maid [15–18]. Clearly, the two models show

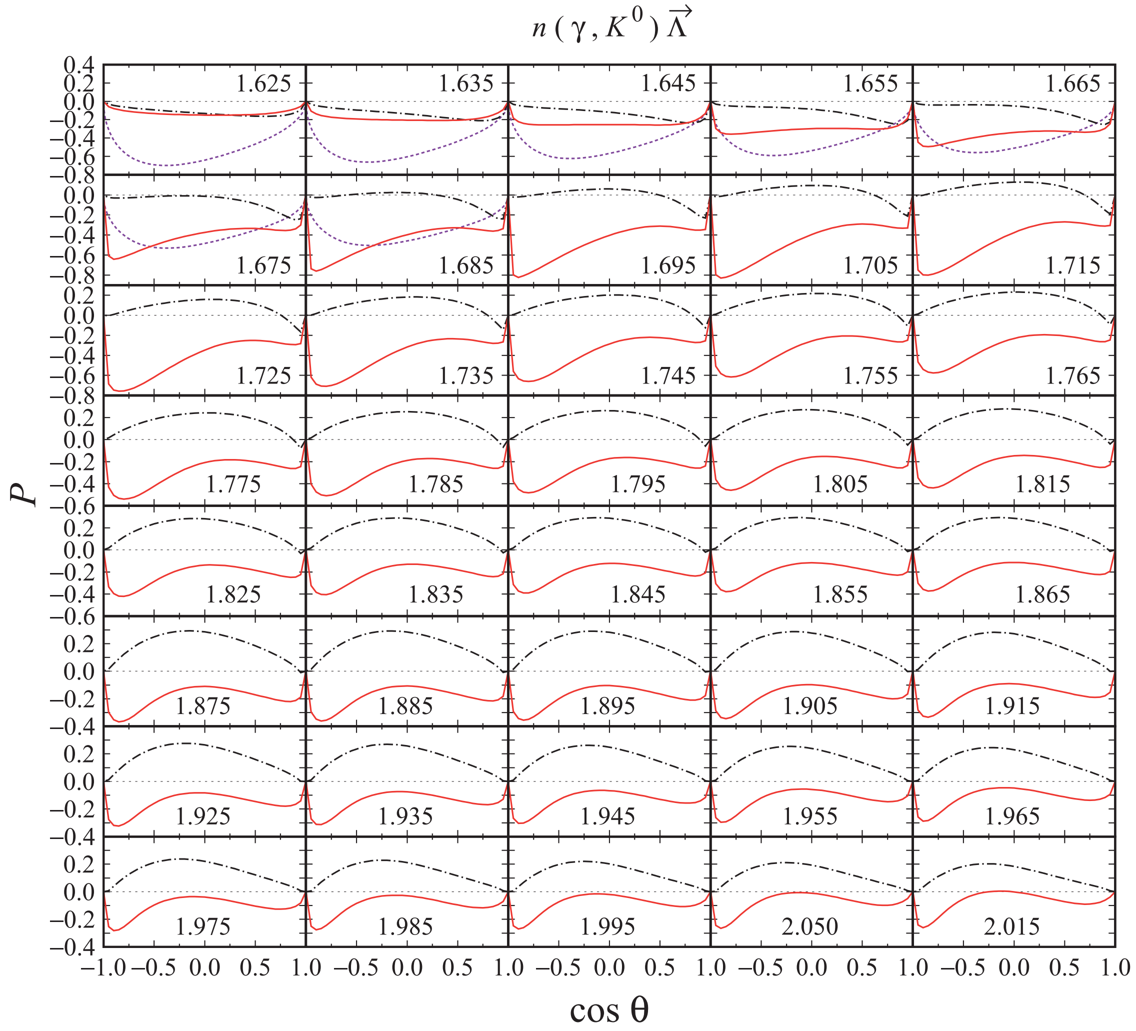

Fig. 17. As in Fig. 16, but for angular distributions. The corresponding total c.m. energy W given in GeV is shown in each panel.

very different results. However, this is understandable because the two models are constructed with different numbers of nucleon resonances and different background configurations. In contrast to the $K^+\Lambda$ channel, the lack of experimental data on the $K^0\Lambda$ channel leads to a large uncertainty in the background and resonance properties. As a consequence, the variance between the multipoles of the two models can also be extremely large, as shown by Fig. 18.

Figure 18 also indicates that compared to the other multipoles the E_{0+} and M_{1+} ones have the largest magnitude. This explains why the largest contribution to the $K^0\Lambda$ total cross section originates from the P_{13} and S_{11} partial waves, as discussed above and shown in Fig. 13.

Finally, we need to mention that the CLAS g14 experiment has measured the $\vec{\gamma}\vec{d} \to K^0\vec{\Lambda}p$ process and all observables for the $\gamma n \to K^0\Lambda$ channel could in principle be extracted. Since the predicted differential cross section and recoil polarization for this channel have been presented and discussed above, we display the remaining 14 polarization observables in Fig. 19, where we have calculated the angular distribution of the observables for $W = 1.750$ and 1.950 GeV, in accordance with the CLAS g14 proposal [61]. Note that there was a sign confusion in the previous works [11,62]. In the present work we follow the sign convention given in Ref. [63], where the previous sign convention

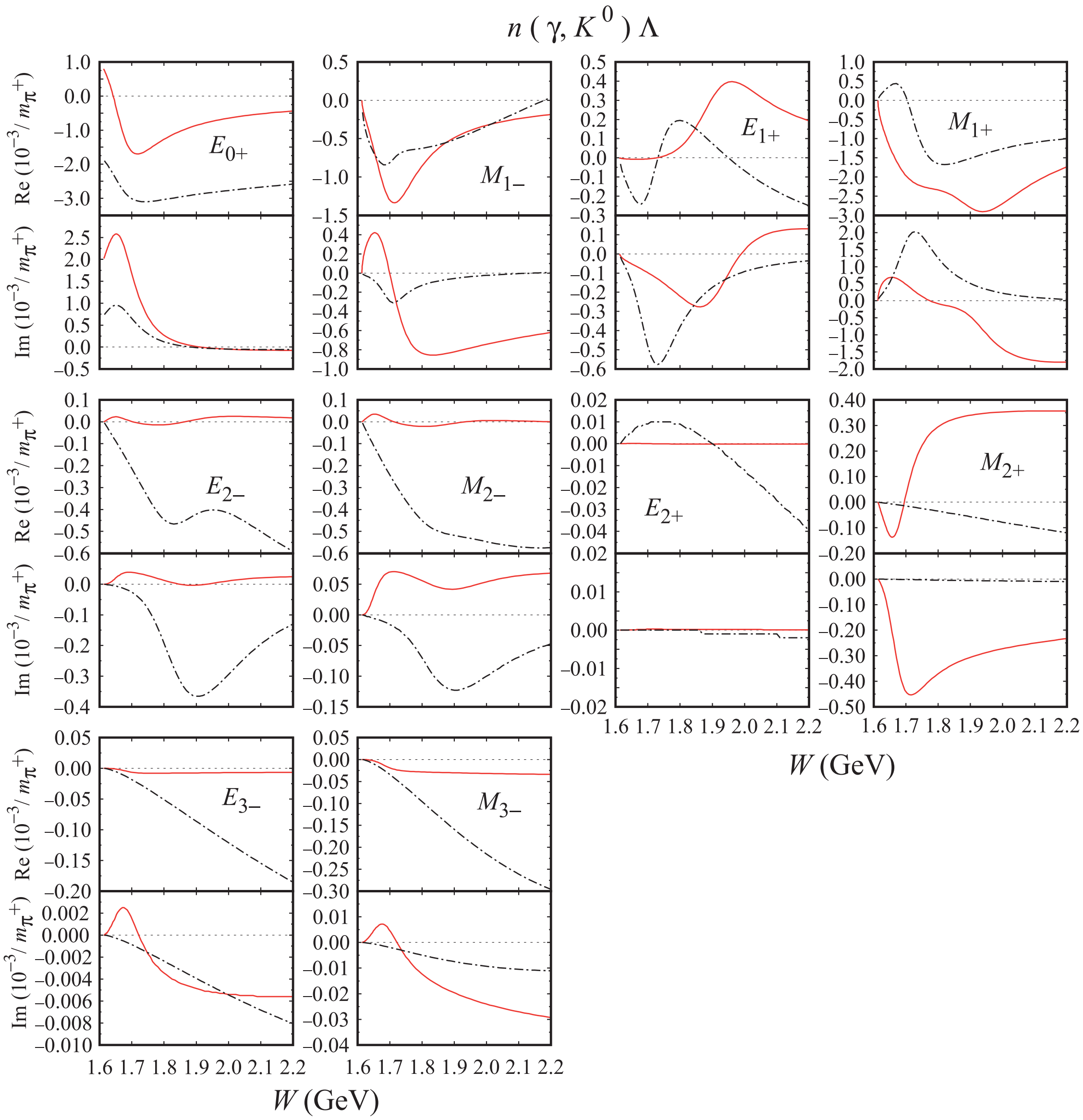

Fig. 18. Calculated electric $E_{\ell\pm}$ and magnetic $M_{\ell\pm}$ multipoles of the nucleon resonances used in the $\gamma n \rightarrow K^0\Lambda$ process. Solid lines display the multipoles obtained in the present work, dash-dotted lines show the multipoles of Kaon-Maid [15–18].

has been corrected. The prediction of Kaon-Maid shown in Fig. 19 has also been corrected to follow this convention. Furthermore, unlike in the previous works, in Fig. 19 we use the meson frame (given in x' and z'; see Ref. [28]) to define the beam-recoil double polarizations $C_{x'}$ and $C_{z'}$, in order to be consistent with the CLAS g14 proposal [61].

As in the case of multipoles, Fig. 19 demonstrates that the two models predict observables with very different shapes and magnitudes. However, this is not too surprising because in the case of recoil polarization we have seen that the predictions of the two models are already completely different (see Figs. 16 and 17). Therefore, we strongly believe that experimental data on the polarization observables extracted from the CLAS g14 experiment will put a stringent constraint on the existing models.

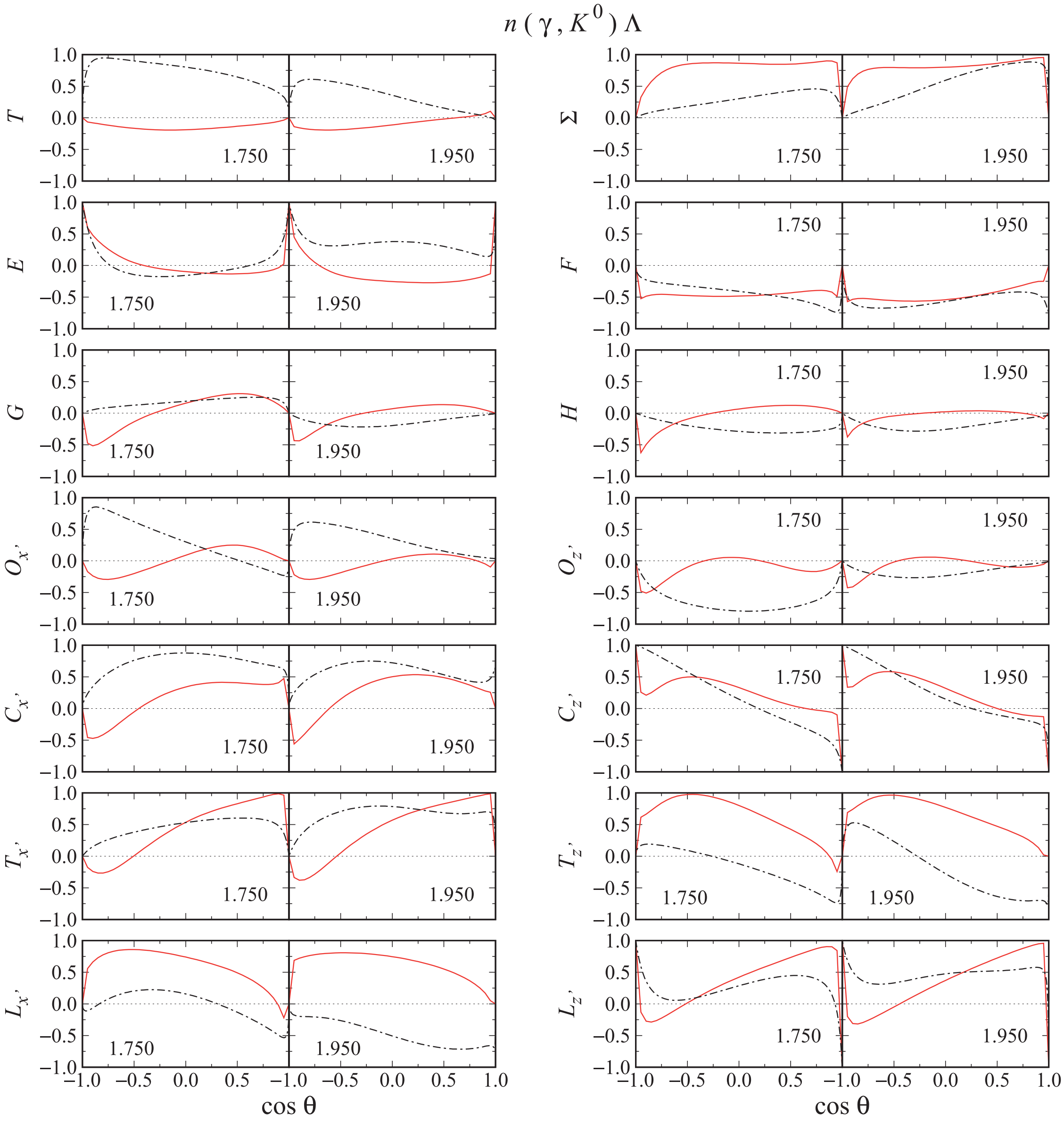

Fig. 19. Angular distributions of single and double polarization observables for the $\gamma n \to K^0\Lambda$ channel obtained in the present work (solid lines) and Kaon-Maid (dash-dotted lines) [15–18]. The corresponding value of the total c.m. energy W (in GeV) is shown in each panel.

5. Summary and conclusion

In this paper we have proposed an isobar model for kaon photoproduction on the proton $\gamma p \to K^+\Lambda$ valid from its threshold up to $W \approx 2.0$ GeV. The model consists of a covariant background amplitude and the Breit–Wigner multipole resonance amplitude. The model can nicely reproduce all available experimental data within the energy range of interest with $\chi^2/N_{\rm dof} = 1.32$. An extensive comparison between model calculations and experimental data shown in this paper proves this result. By exploiting the isospin symmetry and the resonance properties estimated by the PDG we extend the model to predict the observables of neutral kaon photoproduction on the neutron $\gamma n \to K^0\Lambda$ within the same energy range. Unlike the result of $K^+\Lambda$ photoproduction, where the contribution to the cross section is dominated by the resonance amplitude, in the $K^0\Lambda$ photoproduction the dominant contribution comes from the background. In most of the presented kinematics the predicted $K^0\Lambda$ cross sections are larger than the estimates of previous calculations. Two cross section peaks can be observed in the very backward direction. The first peak is centered at $W \approx 1.65$ GeV and originates from the S_{11} partial wave. The second one is centered around $W \approx 1.90$ GeV and originates from the P_{13} partial wave. In the $K^0\Lambda$ photoproduction the largest differential cross section is obtained for $\cos\theta \approx 0.3$ and $W \approx 2.00$ GeV. The calculated Λ polarization exhibits a clear structure at $W \approx 1.70$ GeV. Compared to Kaon-Maid, in most cases the present work predicts polarization asymmetries with different magnitudes and signs, especially for the T, Σ, $O_{x'}$, $O_{z'}$, $C_{x'}$, $T_{x'}$, $T_{z'}$, $L_{x'}$, and $L_{z'}$ asymmetries. The predicted electric and magnetic multipoles are also different from those of Kaon-Maid.

Acknowledgements

This work has been partly supported by the Research-Cluster-Grant of Universitas Indonesia, under contract No. 1862/UN.R12/HKP.05.00/2015 and partly by the PITTA Grant of Universitas Indonesia under contract No. 689/UN2.R3.1/HKP.05.00/2017.

References

[1] M. Kawaguchi and M. J. Moravcsik, Phys. Rev. **107**, 563 (1957).
[2] D. E. Groom and J. H. Marshall, Phys. Rev. **159**, 1213 (1967).
[3] R. Lawall et al., Eur. Phys. J. A **24**, 275 (2005).
[4] H. Kohri et al. [LEPS Collaboration], Phys. Rev. Lett. **97**, 082003 (2006).
[5] S. A. Pereira et al. [CLAS Collaboration], Phys. Lett. B **688**, 289 (2010).
[6] K. Tsukada et al., Phys. Rev. C **78**, 014001 (2008); **83**, 039904 (2011) [erratum].
[7] Y. Tsuchikawa et al., JPS Conf. Proc. **10**, 032010 (2016).
[8] H. Yamamura, K. Miyagawa, T. Mart, C. Bennhold, H. Haberzettl, and W. Glöckle, Phys. Rev. C **61**, 014001 (1999).
[9] A. Salam, K. Miyagawa, T. Mart, C. Bennhold, and W. Glöckle, Phys. Rev. C **74**, 044004 (2006).
[10] C. Patrignani et al. [Particle Data Group Collaboration], Chin. Phys. C **40**, 100001 (2016) and 2017 update.
[11] T. Mart, Phys. Rev. C **82**, 025209 (2010).
[12] T. Mart, Phys. Rev. C **83**, 048203 (2011).
[13] T. Mart, Phys. Rev. C **90**, 065202 (2014).
[14] A. Rusli and T. Mart, AIP Conf. Proc. **1862**, 030007 (2017).
[15] T. Mart, C. Bennhold, H. Haberzettl, and L. Tiator, *An effective Lagrangian Model for Kaon Photo- and Electroproduction on the Nucleon* (Institut für Kernphysik, Universität Mainz, Mainz, 2000). (available at: http://www.kph.uni-mainz.de/MAID/kaon/kaonmaid.html, date last accessed December 11, 2017).
[16] T. Mart and C. Bennhold, Phys. Rev. C **61**, 012201 (1999).
[17] T. Mart, Phys. Rev. C **62**, 038201 (2000).
[18] C. Bennhold, H. Haberzettl, and T. Mart, arXiv:nucl-th/9909022 [Search INSPIRE].
[19] T. Mart and A. Sulaksono, Phys. Rev. C **74**, 055203 (2006).
[20] T. Mart, S. Clymton, and A. J. Arifi, Phys. Rev. D **92**, 094019 (2015).
[21] S. Clymton and T. Mart, Phys. Rev. D **96**, 054004 (2017).
[22] H. Haberzettl, C. Bennhold, T. Mart, and T. Feuster, Phys. Rev. C **58**, R40 (1998).
[23] D. Drechsel, O. Hanstein, S. S. Kamalov, and L. Tiator, Nucl. Phys. A **645**, 145 (1999).
[24] L. Tiator, D. Drechsel, S. Kamalov, M. M. Giannini, E. Santopinto, and A. Vassallo, Eur. Phys. J. A **19**, 55 (2004).
[25] I. G. Aznauryan, Phys. Rev. C **67**, 015209 (2003).
[26] G. F. Chew, M. L. Goldberger, F. E. Low, and Y. Nambu, Phys. Rev. **106**, 1345 (1957).
[27] J. S. Ball, Phys. Rev. **124**, 2014 (1961).
[28] G. Knochlein, D. Drechsel, and L. Tiator, Z. Phys. A **352**, 327 (1995).
[29] H. Thom, Phys. Rev. **151**, 1322 (1966).
[30] V. Sokhoyan et al. [CBELSA/TAPS Collaboration], Eur. Phys. J. A **51**, 95 (2015).

[31] A. V. Anisovich, V. Burkert, E. Klempt, V. A. Nikonov, A. V. Sarantsev, and U. Thoma, Eur. Phys. J. A **49**, 67 (2013).
[32] V. Shklyar, H. Lenske, and U. Mosel, Phys. Rev. C **87**, 015201 (2013).
[33] G. Penner and U. Mosel, Phys. Rev. C **66**, 055211 (2002).
[34] A. V. Anisovich, R. Beck, E. Klempt, V. A. Nikonov, A. V. Sarantsev, and U. Thoma, Eur. Phys. J. A **48**, 15 (2012).
[35] T. Mart and S. Sakinah, Phys. Rev. C **95**, 045205 (2017).
[36] T. Mart and M. J. Kholili, submitted for publication.
[37] R. A. Adelseck and B. Saghai, Phys. Rev. C **42**, 108 (1990).
[38] D. Skoupil and P. Bydžovský, Phys. Rev. C **93**, 025204 (2016).
[39] T. Mart and N. Nurhadiansyah, Few-Body Syst. **54**, 1729 (2013).
[40] F. James and M. Roos, Comput. Phys. Commun. **10**, 343 (1975).
[41] A. I. Nurussalam and T. Mart, AIP Conf. Proc. **1862**, 030004 (2017).
[42] A. I. Nurussalam and T. Mart, to be published.
[43] W. D. Suciawo, S. Clymton, and T. Mart, J. Phys.: Conf. Ser. **856**, 012011 (2017).
[44] W. D. Suciawo, S. Clymton, and T. Mart, to be published.
[45] R. Bradford et al. [CLAS Collaboration], Phys. Rev. C **73**, 035202 (2006).
[46] A. Lleres et al. [GRAAL Collaboration], Eur. Phys. J. A **31**, 79 (2007).
[47] M. E. McCracken et al. [CLAS Collaboration], Phys. Rev. C **81**, 025201 (2010).
[48] T. C. Jude et al. [Crystal Ball at MAMI Collaboration], Phys. Lett. B **735**, 112 (2014).
[49] T. Mart, Phys. Rev. D **83**, 094015 (2011).
[50] T. Mart, Phys. Rev. D **88**, 057501 (2013).
[51] M. Sumihama et al. [LEPS Collaboration], Phys. Rev. C **73**, 035214 (2006).
[52] T. Mart and C. Bennhold, Nucl. Phys. A **639**, 237c (1998).
[53] R. K. Bradford et al. [CLAS Collaboration], Phys. Rev. C **75**, 035205 (2007).
[54] M. Q. Tran et al. [SAPHIR Collaboration], Phys. Lett. B **445**, 20 (1998).
[55] K. H. Glander et al. [SAPHIR Collaboration], Eur. Phys. J. A **19**, 251 (2004).
[56] P. Bydžovský and T. Mart, Phys. Rev. C **76**, 065202 (2007).
[57] T. Mart, Few-Body Syst. **42**, 125 (2008).
[58] A. Lleres et al. [GRAAL Collaboration], Eur. Phys. J. A **39**, 149 (2009).
[59] P. A. Carruthers, *Introduction to Unitary Symmetry* (Wiley, New York, 1966).
[60] T. Mart, C. Bennhold, and C. E. Hyde-Wright, Phys. Rev. C **51**, R1074 (1995).
[61] A. Sandorfi (spokesperson), JLab proposal PR-06-101: N^* Resonances in pseudoscalar-meson photo-production from polarized neutrons in $\vec{\mathrm{H}} \cdot \vec{\mathrm{D}}$ and a complete determination of the $\gamma n \to K^0 \Lambda$ amplitude (available at: https://www.jlab.org/exp_prog/proposals/06/PR06-101.pdf, date last accessed December 11, 2017).
[62] A. M. Sandorfi, S. Hoblit, H. Kamano, and T.-S. H. Lee, J. Phys. G **38**, 053001 (2011).
[63] R. L. Workman, L. Tiator, Y. Wunderlich, M. Döring, and H. Haberzettl, Phys. Rev. C **95**, 015206 (2017).